



**HAL**  
open science

# Multiscale Morphological and Electrical Characterization of Charge Transport Limitations to the Power Performance of Positive Electrode Blends for Lithium-Ion Batteries

Nicolas Besnard, Aurélien Etienne, Thierry Douillard, Olivier Dubrunfaut, Pierre Tran-Van, Laurent Gautier, Sylvain Franger, Jean-Claude Badot, Eric Maire, Bernard Lestriez

► **To cite this version:**

Nicolas Besnard, Aurélien Etienne, Thierry Douillard, Olivier Dubrunfaut, Pierre Tran-Van, et al.. Multiscale Morphological and Electrical Characterization of Charge Transport Limitations to the Power Performance of Positive Electrode Blends for Lithium-Ion Batteries. *Advanced Energy Materials*, 2017, 7 (8), pp.1602239. 10.1002/aenm.201602239 . hal-03538479

**HAL Id: hal-03538479**

**<https://hal.science/hal-03538479>**

Submitted on 21 Jan 2022

**HAL** is a multi-disciplinary open access archive for the deposit and dissemination of scientific research documents, whether they are published or not. The documents may come from teaching and research institutions in France or abroad, or from public or private research centers.

L'archive ouverte pluridisciplinaire **HAL**, est destinée au dépôt et à la diffusion de documents scientifiques de niveau recherche, publiés ou non, émanant des établissements d'enseignement et de recherche français ou étrangers, des laboratoires publics ou privés.

DOI: 10.1002/ ((please add manuscript number))

**Article type:** Full paper

**Multiscale morphological and electrical characterization of charge transport limitations  
to the power performance of positive electrode blends for lithium-ion batteries**

*Nicolas Besnard, Aurélien Etienne, Thierry Douillard, Olivier Dubrunfaut, Pierre Tran-Van,  
Laurent Gautier, Sylvain Franger, Jean-Claude Badot, Eric Maire, Bernard Lestriez\**

Dr. N. Besnard, Dr. B. Lestriez

Institut des Matériaux Jean Rouxel (IMN), CNRS UMR 6502, Université de Nantes, 44322,  
Nantes Cedex 3, France.

E-mail: [Bernard.Lestriez@cnrs-immn.fr](mailto:Bernard.Lestriez@cnrs-immn.fr)

Dr A. Etienne, Dr T. Douillard, Dr E. Maire

Laboratoire MATEIS, CNRS UMR5510, Institut national des sciences appliquées de Lyon, F-  
69621 Villeurbanne, France.

Dr. O. Dubrunfaut

Laboratoire de Génie Electrique de Paris, CNRS, SUPELEC, Sorbonne Universités-UPMC  
Univ., Paris 06, Univ. Paris-Sud, 11 rue Joliot-Curie, Plateau de Moulon, 91192, Gif-sur-  
Yvette, France.

Dr. N. Besnard, Dr P. Tran-Van

Renault Technocentre, DEA-IR, 78084 Guyancourt, France.

Dr. L. Gautier

Umicore Rechargeable Battery Materials, 1000 Brussels, Belgium.

Prof. S. Franger

ICMMO-ERIEE (UMR 8182), Université Paris Sud, 15 avenue Georges Clémenceau, 91045  
Orsay, France.

Dr. J.-C. Badot

Chimie ParisTech, PSL Research University, CNRS, Institut de Recherche de Chimie Paris,  
75005 Paris, France.

**Keywords:** lithium-ion batteries; composite electrodes: ionic and electronic wirings; 3D  
geometry; power performance.

**Abstract** - In this work, exhaustive characterizations of 3D geometries of  $\text{LiNi}_{1/3}\text{Mn}_{1/3}\text{Co}_{1/3}\text{O}_2$  (NMC),  $\text{LiFePO}_4$  (LFP), and NMC/LFP blended electrodes are undertaken for rational interpretation of their measured electrical properties and electrochemical performance. X-Ray tomography and Focused Ion Beam in combination with Scanning Electron Microscopy (FIB-SEM) tomography are used for a multiscale analysis of electrodes 3D geometries. Their multiscale electrical properties are measured by using Broadband Dielectric Spectroscopy (BDS). Finally, discharge rate performance are measured and analyzed by simple, yet efficient methods. It allows discriminating between electronic and ionic wirings as the performance limiting factors, depending on the discharge rate. This approach allows a unique exhaustive analysis of the experimental relationships between the electrochemical behavior, the transport properties within the electrode and its 3D geometry.

## 1. Introduction

Lithium-based batteries (LIB) have higher energy density and cycle life compared to other battery systems. [1] The demand for LIB with higher gravimetric and volumetric energy density is growing to extend the operation hours of mobile information technology (IT) devices, the driving mileages of all-electric vehicles, and due to the rapidly increasing integration of renewable energy into the global energy scheme. [2,3] This way, optimizing cell designs and electrode engineering is now well identified as being a (or even more the) main issue by both industrial and academic bodies. [2,3,4,5,6] Indeed, in commercial batteries, practical electrodes must be made thin to show acceptable power. As a result, 50% of batteries weight and volume are non electroactive materials. Consequently, LIB for Electrical Vehicles (EV) are locked on a trade-off between energy (autonomy) and power (charge rate).

Although industrial-grade active materials such as Graphite,  $\text{LiFePO}_4$  (LFP) or  $\text{LiNi}_{1/3}\text{Mn}_{1/3}\text{Co}_{1/3}\text{O}_2$  (NMC) are intrinsically capable of very fast lithium (de)insertion, [7,8,9] several factors limit their rate (power) performance when formulated as thick electrodes. [10,11,12,13,14,15,16] These factors, which affect the rate of lithium and electron supplies to the active mass, also called the ionic and electronic wirings, depend on the architecture (nano- and microstructure) of the electrode through the interfacial areas, materials connectivity, and the transport length scales.

Novel opportunity for progressing in this direction and explore relationships between electrode architecture and electrochemical performance is implementation of X-ray computed tomography (XRCT) [17,18,19,20,21,22,23,24,25,26] and focused ion beam in combination

with scanning electron microscopy (FIB-SEM) [27,28,29,30,31] techniques to characterize and quantify the 3D architecture of composite electrodes. XRCT is non-destructive technique that allows probing large volumes covering the entire electrode thickness, which is necessary for reliable analysis. However, one disadvantage of XRCT is the difficulty of distinguishing the carbon additive and the binder mixture from the pore space due to the small particle size and the low X-ray absorbance of the carbon and binder mixture. FIB-SEM is destructive but has the ability to provide 3D imaging at high enough spatial resolution. The combination of XRCT and FIB-SEM is then method of choice for exhaustive multi-scale description of electrode 3D geometry. [32,33]

XRCT and FIB-SEM thus enable to extensively analyze a number of geometric parameters (volume fraction, surface area, particle size distribution, tortuosity...), which is of great potential to rationally design and optimize the formulation and the processing of composite electrodes. In particular, tortuosity, which is identified as critical parameter with respect to ionic transport, has been exhaustively studied with respect to its calculation method and the influence of particles shape and orientation, and electrode inhomogeneities. [22,24,25,30,34] Comparatively, factors that play on the electrons transport and distribution to the active mass have been much less considered. [35] Moreover and surprisingly, attempts to correlate quantified 3D geometries with measured electrochemical power performance [19] or electrical transport properties [36] of same real electrodes remain rare or modest. In general, reconstructed geometries are used to calculate effective transport properties and make assumptions about the main limitations to rate performance. Intensive work is now undertaken to use reconstructed 3D geometries for smarter electrochemical modelling than the state-of-the-art modelling based on idealized microstructures, [37,38,39,40] but still with very little or even no confrontation with measured electrochemical performance. Although significantly improved by considering the spatial distribution of the different phases, the efficiency of this approach remains nevertheless controversial as several of the models parameters remain assumed (for example the electrical conductivity of the electrode materials and the charge transfer reaction factors) and the influence of the inter-connectivity between the CB/binder network and the active mass is generally not considered. Moreover very long simulation times are required.

In this work, exhaustive characterizations of 3D geometries of NMC, LFP, and NMC/LFP blended electrodes are undertaken for rational interpretation of their measured electrical properties and electrochemical performance. Blending different active materials is an approach intensively followed by automotive battery suppliers intended to optimize the

battery performance with respect to the automotive operating requirements. Motivations are to achieve a more balanced performance compared to what is possible with any individual compound, and to minimize the shortcomings of the parent materials. [41] It has been reported that the blending of NMC with LFP may improve the thermal stability and the electrochemical performance in terms of discharge capacity, cycle stability, and rate capability. [42] The pulse power capability of Lithium- and manganese-rich transition metal layered-oxides (LMR-NMCs) at low State-of-Charge (SoC) is also improved by incorporating a modest quantity of LFP. Very few works on blended positive electrodes paid attention, however, to the influence of the electrode engineering on electrochemical behavior. [43,44,45]

## 2. Results

### 2.1. Electrode morphology

Due to space limitation the experimental section is given in Supporting Information (SI), which is divided in several sections: materials (SI1), tomography observations (SI2), morphological quantifications (SI3), electrical measurements (SI4), electrochemical measurements (SI5). **Table 1** gives the electrodes composition, average porosity and thickness. 3D geometry quantitative analysis was performed from X-ray and FIB/SEM tomography reconstructions following a set of previously developed methods. [22,26,35,46] Additional information about this set of electrodes can be found in previous papers that analyze the homogeneity of the samples [47,48] Here we focus on morphological parameters that have been found the more relevant for interpretation of the electrical properties and the electrochemical performance. FIB-SEM reconstructions of electrodes A (NMC), F (NMC/LFP), H (NMC/LFP) and J (LFP) are shown in **Figure 1**. Morphological parameters extracted from these analyses are reported in **Table 1**, and **Figure 2** and **3**.

#### 2.1.1 Connectivity of the different materials and phases

In electrode A (NMC), the packing of the large spherical NMC particles (about 10 $\mu$ m in size) determines micrometric porous interstices (**Figure 1a-b**). The PVdF binder and carbon black (CB) particles are coagulated together. This mixture forms micrometer thick strands spreading throughout the electrode gluing the NMC particles and partially filling the pores. The intra-connectivity<sup>1</sup> of this CB+PVdF mixture reaches 77%. The inter-connectivity

---

<sup>1</sup> The intra-connectivity is quantified as the volume fraction of the most voluminous cluster of one material/phase in the analyzed volume; a value of 100% meaning all voxels of this material/phase being part of a same unique network.

<sup>2</sup> between NMC and CB+PVdF represents only 13% of the NMC surface and 8% for the CB+PVdF mixture, the rest of their surface being exposed to porosity (**Figure 2f**). Thus, 87% of the NMC surface should be in contact with the electrolyte when it fills the porosity after battery assembly. The pores are large, between ten nanometers and about 1600nm with a median pores size at ~400nm (**Figure 3a**), and well-connected (100% intra-connectivity).

In electrodes J (LFP), the packing of the nanometric LFP particles, some of them being aggregated in clusters of particles of a few micrometers, determines well-connected pores of size between ten nanometers and about 800nm with a median pores size at ~100nm (**Figure 3a**). The surface fraction of LFP in contact with electrolyte should be high (LFP/porosity inter-connectivity is 90%, **Figure 2e**). However, the CB+PVdF mixture is scattered within the network of LFP particles and does not percolate (CB+PVdF intra-connectivity is only 25%, **Table 1**). This is expected given the particle size ratio of LFP and CB particles close to unity. <sup>[49]</sup>

The blended NMC/LFP electrodes (F and H) have morphologies that resemble to the LFP electrode but with NMC particles distributed inside. Indeed, the strands of CB+PVdF mixture and the pores (**Figure 3a**) exhibit a nanometric range of size. Moreover, LFP and CB+PVdF mixture appear well mixed. As a matter of fact, the CB+PVdF mixture has about one-third of its specific surface in contact with LFP for both electrodes (**Figure 2f**). This homogeneous intermixing of these components may be related to some attractive interactions between the CB and the carbon coated LFP particles in the electrode slurry, as well as between the PVdF chains and the carbonaceous surfaces, [50] and to a repulsive interaction between PVdF and oxygen rich NMC surface. [51] The nanometric strands of CB+PVdF, are much well intra-connected through the network of LFP particles than in J, with values of 88% and 92% for F and H, respectively (**Table 1**), because the CB+PVdF mixture is excluded from the volume occupied by NMC and is thus more concentrated in the LFP/CB+PVdF mixture than in J. However, as a consequence of the LFP/CB+PVdF intermixing, only 2.6% of the NMC surface is connected with the CB+PVdF phase in H, which is 5 times less than in A, although both samples have same CB+PVdF contents (8wt%). Increasing this content to 12wt% in F allows increasing the NMC inter-connectivity with CB+PVdF to 8%. The inter-connectivity of the LFP phase with the CB+PVdF mixture is also lower in H (13%) compared to F (23%), for same reason. If 15-17% of the NMC surface is in contact with the LFP phase in the two electrodes, it represents however a very small specific surface area fraction of LFP

---

<sup>2</sup> The inter-connectivity was characterized by identifying the common outlines of the different materials/phases and quantifying the specific surface area fraction of each material/phase in contact with another material/phase.

(<1%) (**Figure 2e-f**). Pores are well-connected in both NMC/LFP electrodes (100% intra-connectivity, **Table 1**). Pores size (**Figure 3a**) is included between a few ten nanometers up to about 800nm with a median pores size at ~130nm in electrode F. It is lower in H due to the bench-top hydraulic densification.

### 2.1.2 Tortuosity of the porosity

Physically, pore tortuosity is defined as the ratio of the actual distance travelled by the species per unit length of the medium. It is a measure for the elongation of a transport path due to the twisty structure of the pores imposed by the presence of the solid electrode matter. It influences the liquid phase transport of electrolyte species, as expressed in the relationship of the intrinsic diffusion coefficient  $D_0$  in a non-tortuous path and the effective one  $D_{eff}$  [52,53]

$$D_{eff} = D_0 \frac{\varepsilon}{\tau^2} = D_0 \frac{\varepsilon}{T} \quad (1)$$

where  $\varepsilon$  is the porosity,  $\tau$  the tortuosity and  $T$  the tortuosity factor. Note that  $T$  is often confused to  $\tau$  in the literature. The well-known Bruggeman relationship is often used to relate the tortuosity to the porosity: [24,34,52,53]

$$T = \tau^2 = \gamma \varepsilon^{1-\alpha} \quad (2)$$

where  $\alpha$  (Bruggeman coefficient) and  $\gamma$  are constants. It is generally assumed that  $\gamma=1$  and  $\alpha=1.5$  in battery models. However, higher  $\gamma$  and/or  $\alpha$  values have been obtained from experimental and simulation methods. Comparison of the tortuosity factors determined in previous investigations shows a large dispersion, even considering same electrode materials, and it appears that the method used to quantify the tortuosity has a major influence. As a rule, higher tortuosity factors are obtained by solving diffusion equation through finite element simulation, [18,21,23,25] porosimetry [52] or electrochemical measurements, [53] while lower values are determined by geometrical calculations. [17,22,23,28,54] In the case of electrodes with at least two populations of widely different sizes, the contributions of both the tortuosity of coarse and fine architectures have to be considered. The electrode tortuosity factor can be expressed as [55]

$$T_t = T_o T_v \quad (3)$$

where  $T_o$  is the microscale tortuosity factor of the electrode layer and  $T_v$  is the nanoscale tortuosity factor. This expression takes into account the ‘‘amplifying effect of the microporosity on the macroporous backbone’’. [55] In this paper, the tortuosity factor has been investigated by geometrical calculation but following a directional distance map

propagation method, [54] which provides good-agreement with the effective diffusion-based tortuosity values. [22] Moreover, this method provides a more complete description of the tortuosity distribution as spatial distribution map.  $T_0$  has been estimated from X-ray tomography reconstructions by considering the deviations imposed by NMC particles only for propagation through the electrode; and  $T_v$  has been calculated for the pores distinguished by FIB-SEM tomography (**Table 1**). Bruggeman coefficient  $\alpha_t$  was then calculated by the combination of equations 2 and 3 (see detailed calculation in SI3 and values in **Table 1**) for being used in appreciation of electrochemical performance (see below equation 6).

In electrode A (NMC), microscopic tortuosity factor (**Table 1**) is estimated at 1.22. Average nanoscale tortuosity factor is estimated at 2.10, which gives a Bruggeman coefficient of 1.35 to characterize the electrode at this scale. Tortuosity is however strongly dependent on the initial seed plane and the labelled trajectories direction, due to the anisotropic pore morphology (**Table S1**). However, some key morphological features can be identified looking at profile of the nanoscale tortuosity factor through the electrode thickness (**Figure 3b**, with initial starting plane close to electrode surface), and associated 2D cartography (**Figure 3c**). Firstly, labelled trajectories followed through the pores have to pass around the large NMC particles, which results in high local tortuosities ( $T_v > 2$ ). Secondly, the CB+PVdF mixture clusters induce a large range of pore size (**Figure 3a**), which leads to important tortuosity heterogeneities in agreement with previous works. [30,31,33b,36] The large cavities favour low tortuosity ( $T_v = 1.2-1.5$ ), while tiny pores within the CB+PVdF mixture or at the interface between NMC particles and CB+PVdF mixture are characterized by high tortuosity ( $T_v = 1.7-2.5$ ). Using equations 2 and 3, a mean Bruggeman coefficient of 1.54 is estimated as characteristic of the whole electrode, which takes into account the contribution of the coarse and fine structures. In electrode J (LFP), tortuosity is low ( $T_v = 1.25$ , **Table 1**) and rather homogenous (**Figure 3b and f**). Such values obtained by geometrical calculation appear lower than the one estimated in previous investigations of LFP electrodes, [23,28,53] which may be due to the geometrical calculation that tends to provide low tortuosity values [54,56,57], but also to the spherical shape and narrow size distribution of the LFP particles studied here. [24] The CB+PVdF cluster observed on the bottom right however induces local tortuosity heterogeneity due to its larger size than LFP particles and low porosity. A mean Bruggeman coefficient of 1.20 is estimated as characteristic of this electrode. For NMC/LFP blends, the contribution of the tortuosity factor of coarse and fine structures has to be considered. In as-received NMC/LFP electrode F, nanoscale pores tortuosity factor is constant through the thickness (**Figure 3b**). The 2D representation (**Figure 3d**) shows rather

homogeneous tortuosity in the nanometric pores, scattered in the LFP/CB+PVdF mixture, while variations with higher values are observed around the NMC secondary particle. A mean Bruggeman coefficient of 1.34 is estimated as characteristic of the whole electrode. For the super-calendered NMC/LFP electrode H, the nanoscale tortuosity factor is slightly higher than the as-received NMC/LFP electrode F (**Figure 3b**). In addition, the 2D representations (**Figure 3e**) show more heterogeneities. However, direct comparison between F and H shall take into account the fact that they have different additives contents. As in electrodes A and F, higher tortuosity is observed at the junctions between the mixture of nanometric LFP particles with CB+PVdF mixture and the micrometric NMC particles. The cracking of the latter during the bench-top hydraulic pressing of H leads to the formation of interstices between the NMC grains, which also locally highly increase tortuosity. Compared to F, there are also tortuosity heterogeneities in the nanoscale pores, which may be associated with the decreases of the pore size and pathways number due to super-calendering. A Bruggeman coefficient of 1.30 is estimated as characteristic of the whole electrode. In summary, NMC and NMC/LFP electrodes architectures are characterized by geometrical Bruggeman coefficient of about 1.53 to 1.35 with respect to their pores tortuosity, which is a higher value than 1.2 found for the LFP electrode. This difference is due to the mismatch between the micrometric NMC and the nanometric CB or LFP particle sizes that induces detrimental large deviations for ionic paths in the corresponding electrodes.

### 2.3 Electrical properties

Real part of the complex conductivity,  $\sigma'$ , as a function of the frequency is shown in **Figure 4a,b** for various electrodes A and B (NMC); F, G and H (NMC/LFP); J, K and L (LFP). The study of the temperature dependence and the analysis of Nyquist plots (see SI and also methodology in previous works [58,59,60,61]) allowed to extract several well defined electrical properties (**Table 1**): the contact resistance,  $R_C$ , between the electrode layer and the aluminum current collector and the electronic conductivity of the electrode layer,  $\sigma_{dc}$ , which is first discussed.

Conductivity of NMC electrodes A and B (8 to 10.7S.m<sup>-1</sup>, **Table 1**) is much higher than the NMC powder (4.9.10<sup>-4</sup>S.m<sup>-1</sup> for pressed pellet), due to the CB addition and percolation in the electrode. The temperature independence of  $\sigma_{dc}$  is characteristic of metal-like electrical behavior (activation energy  $\approx$  0eV in **Table 1**), which shows that the CB+PVdF mixture percolates and short-circuits the less conductive NMC particles in the electrode. This behavior is related to the high intra-connectivity of the CB+PVdF mixture (77%) quantified

from FIB/SEM images. The behavior of LFP electrodes J and K is more complex. Decomposition of the high frequency part of the electrical spectra gives two conductivities. First one, in the  $10^6$ - $10^7$ Hz frequency range, is the electronic conductivity of the electrode layer,  $\sigma_{dc}$ , with values of 0.31 and 0.60S.m<sup>-1</sup> and activation energy of 0.07eV that are close to the values obtained for pressed pellet of LFP powder (0.26S.m<sup>-1</sup> and 0.09eV). This comparison confirms that the CB+PVdF mixture does not percolate, in agreement with low intra-connectivity of only 25% in the case of J as determined from FIB/SEM reconstructions. The electrical conductivity in LFP electrodes J and K is mainly insured by the intra-connectivity of LFP particles and thus by the carbon coating percolation.<sup>[60]</sup> The signature of isolated CB+PVdF clusters is however seen at very high frequency (see SI4) with a second conductivity value of 4.1 and 6.3S.m<sup>-1</sup> (in J and K) showing no dependence with the temperature (activation energy  $\approx$  0eV, **Table 1**). Increasing the CB content in the NMC electrode (B) does not bring significant change to  $\sigma_{dc}$  (**Table 1**), likely because the CB+PVdF mixture percolation is already achieved in A. Contrarily, increasing the CB content in the LFP electrode (L) brings significant improvements to the electrical properties (**Table 1** and **Figure 4b**), likely reflecting an improvement in the CB+PVdF intra-connectivity.

Similarly, the NMC/LFP electrodes H and F show electrical properties typical of percolated CB+PVdF network (see SI4), which is also well in agreement with high intra-connectivity of the CB+PVdF mixture ( $\sim$ 90%). The NMC/LFP electrode H and the NMC electrode A have the same CB amount (in wt% and in v%, **Table 1**) and good intra-connectivity of the CB+PVdF mixture, which is however higher for H compared to A, e.g. 92 vs. 77% (**Table 1**). Nevertheless, the electrode film conductivity is lower for H, e.g. 3.4 vs 8.0S.m<sup>-1</sup>. Such a result could be due to the larger size of the CB+PVdF mixture strands in NMC electrode (A) that form thicker (although less numerous) conducting paths than in NMC/LFP electrode H, possibly because the occurrence of resistive defects interrupting the current paths is more likely to happen in network with thinner strands. NMC/LFP electrode F has a higher CB content than H, e.g. 5.8 vs 3.9v%, and shows thus higher electrode conductivity, e.g. 8.1 vs 3.4S.m<sup>-1</sup>. However it is interesting to note that the CB+PVdF mixture strands have same thickness in both electrodes. This way, the higher conductivity in F could be attributed to more numerous conducting paths, due to higher CB+PVdF mixture content, than in H.

A novel parameter to qualify the contact at the current collector/electrode interface is introduced. The contact resistance is given as  $R_c = R_{CR} + R_f$ , where  $R_{CR}$  is the constriction resistance and  $R_f$  is the resistance of the oxide film present at the extreme surface of the

aluminum foil. [62,63]  $R_f$  is not expected to vary with the electrode composition. The constriction resistance  $R_{CR}$  is expected to vary as

$$R_{CR} \propto 1/(\sigma_{dc} \times \Sigma) \quad (4)$$

where  $\sigma_{dc}$  is the electrode mixture conductivity and  $\Sigma$  is the areal density of contact points at the collector/electrode interface. [64]  $R_C$  and  $\sigma_{dc}$  are plotted in **Figure 4c** for selected electrodes having close CB content of 3.5-4.2%v.  $\sigma_{dc}$  regularly increases in the following order K (LFP), G (NMC/LFP), H (NMC/LFP) and A (NMC), in agreement with the CB volumic ratio in the mixture. However,  $R_C$  does not follow this regular variation, as it displays maximum values for the G. The quantity  $1/(\sigma_{dc} \times R_C)$  that should be proportional to  $\Sigma$  is plotted in **Figure 4d** to relate  $R_C$  and the different electrode morphologies. Low  $R_C$  of electrode K (LFP) and further increase of  $R_C$  with the decrease of LFP and the proportional increase of NMC contents in G can be attributed to the numerous contact points that the LFP particles can make at the surface of the current collector in addition to CB ones. [63] As the LFP nanoparticles content are progressively replaced by micrometric NMC particles, the areal density of contact points at the interface naturally decreases and thus  $R_C$  increases. At highest NMC contents (in A), dramatic decrease of  $R_C$  and increase of  $\Sigma$  can be explained by an accumulated layer of CB+PVdF, due to a processed induced rheological migration phenomenon. [48]

Comparison of J and K or of G and H, illustrates the influence of super-calendering. In the case of LFP electrodes, it can be seen that the electrode mixture as well as the isolated CB clusters conductivity slightly increase from 0.305 to 0.601 S.m<sup>-1</sup> and from 4.1 to 6.3 S.m<sup>-1</sup>, respectively, but the contact resistance significantly decreases from 36 to 0.8 Ω.cm<sup>2</sup> from J and K, which can be attributed to an increase of  $\Sigma$  (from 9.2 to 208 a.u.) (**Table 1**). For the NMC/LFP electrode G, as for LFP electrode J and K, two conductivities were extracted; the electrode mixture conductivity at lower frequency and some isolated CB+PVdF clusters at higher frequency, suggesting that percolation of the CB+PVdF mixture was hardly achieved. However, super-calendering this electrode to form H resulted in the disappearance of the signature of isolated CB+PVdF clusters. Nevertheless, the electrode conductivity only slightly increases from 2.4 to 3.4 S.m<sup>-1</sup>, but the contact resistance significantly decreases from 7.5 to 0.64 Ω.cm<sup>2</sup> from G and H, which can be attributed to an increase of  $\Sigma$  (from 5.6 to 45.5 a.u.) (**Table 1**).

## 2.4 Electrochemical measurements

Typical discharge curves of NMC electrodes (A and B), LFP (J and K) and NMC/LFP (F, G and H) at various C-rates and surface capacities of  $2.6\text{mAh}\cdot\text{cm}^{-2}$  are shown in **Figure 5a-c**. Considering the best electrode A, NMC delivered a reversible discharge capacity of  $158\text{mAh}\cdot\text{g}^{-1}$  at C/20 and  $95\text{mAh}\cdot\text{g}^{-1}$  at 2C. In electrode J, LFP delivered a low capacity, which can be attributed to the very high contact resistance for this sample (**Table 1**) that results in strong polarization even at very low rate. [63] Super-calendering J (to form K) results however in discharge capacity of  $157\text{mAh}\cdot\text{g}^{-1}$  at C/20 and  $46\text{mAh}\cdot\text{g}^{-1}$  at 2C. It is generally assumed that carbon-coated LFP is capable of sustaining high-rate discharge currents. [41,42] The degree of polarization is however larger and the discharge capacity lower in K (LFP) than in A (NMC), although both have same weight fraction of CB+PVdF mixture. This under performance of LFP in K can be attributed to the lack of intra-connectivity of the CB+PVdF mixture that results in low conductivity of the electrode and thus poor electronic wiring of the active mass. Such a behavior might appear in contradiction with the high intrinsic electronic conductivity of the LFP powder ( $0.26\text{S}\cdot\text{m}^{-1}$  for a pellet, SI4). But recent works suggest the electronic conductivity within the carbon coating is likely hindered when LFP is wetted by the electrolyte, as a consequence of interactions between lithium ions and electrons within the carbon coating. [65] This is confirmed in SI5 (**Figure S7c,d**) where are compared the performance of electrodes K and L (but with surface capacities of  $1.8\text{mAh}\cdot\text{cm}^{-2}$ ). In L the CB content of 4.5wt% allows to achieve high electrode conductivity and much better rate performance. For NMC/LFP electrodes the discharge curves occur in two steps showing the electrochemical signature of both active materials, the distinct plateau of LFP appearing after the sloppy voltage decline of NMC. Best electrode F delivered reversible discharge capacity of  $159\text{mAh}\cdot\text{g}^{-1}$  at C/20 and  $82\text{mAh}\cdot\text{g}^{-1}$  at 2C, which represents an intermediate behavior between NMC and LFP (A and K) electrodes. Furthermore, discharge capacity as a function of the C-rate is shown in **Figure 5d-f**. For NMC/LFP electrodes, the capacity delivered by each material ( $Q_{\text{NMC}}$  and  $Q_{\text{LFP}}$ ) to the total discharge capacity at a given rate was determined from charges measured at the slow C/5 rate followed by a floating period ( $Q = Q_{\text{NMC}} + Q_{\text{LFP}} + Q_{\text{floating}}$ ) see **Figure S9b**. The capacity  $Q_{\text{floating}}$  recovered during the floating period is significant in the case of electrode H as a consequence of large polarization in charge even at C/5 rate.

A critical discharge rate,  $C^*$ , is observed (marked by an arrow), except for electrode J. It appears as an elbow where the slope of the discharge curve markedly increases. Also known as maximum working rate, [66]  $C^*$  identifies two different limitation regimes. Above  $C^*$ , it is now well accepted that rate performance is controlled by the lithium ion diffusion

resistance within the electrolyte in the electrode porosity [66,67,68,69,70,71,72]. The large mismatch between the lithium concentration in the electrolyte and the active material concentration in the electrode, and the limited lithium ion diffusion kinetics into the electrolyte lead to the depletion of lithium ions inside the electrode porosity at some point, and a brutal decrease in cell voltage that ends the discharge. Below  $C^*$ , it is considered that the electrode resistance,  $R_{\text{electrode}}$ , is the limiting factor. [16,69b,73,74] It gathers several contributions reflecting several steps: (i) the transport of electrons and ions from their “reservoirs” to the active particles, (ii) the charge incorporation reaction which involves the transfer of both charged species from the outside into the interior of active particles and (iii) the transport of lithium specie inside the solid active particles. [73] The electronic wiring of the active mass affects (i) through the contact resistance at the electrode/current collector interface [63,75] and the electrical resistance of the CB network, and (ii) through the areal density of contact points or contact surface area between the active particles and the CB network. [76,77,78,79,80,81]. The ionic wiring of the active mass affects (i) through the electrical resistance of the pores network, [72,73] and (ii) through the accessibility of the liquid electrolyte to the active mass surface (which can be covered by poorly ionic conductor material such as the binder or some liquid electrolyte degradation species). [82,83]

Influence of the electrode parameters on the rate performance is conveniently assessed through a time constant,  $k$  (in hours), [69,70,84,85] which is obtained from the relationship between the discharge capacity  $Q$  (in mAh.g<sup>-1</sup>) and the specific discharge current  $I$  (in mA.g<sup>-1</sup>):

$$Q = Q_0 - k \times I \quad (5)$$

where  $Q_0$  is the discharge capacity extrapolated to very low current.  $k$  is the capacity loss coefficient with respect to  $I$ .  $k_1$  and  $k_2$  can be defined below and above  $C^*$ , respectively. Their variations with the temperature were studied in the case of electrode A and K (see **Figure S6d**). If  $k_2$  is determined by lithium ion diffusion kinetics into the electrode porosity, then it is expected to scale inversely with the effective diffusion coefficient of lithium ions inside the electrode,  $D_{\text{eff}}$ , given by Equation (1). [69,70] In a limited temperature range, the diffusion variation with the temperature can be expressed by Arrhenius equation that gives: [86]

$$\ln(1/k) = \ln(1/k_0) - E_a/k_B T \quad (6)$$

with  $E_a$  the activation energy (in eV),  $k_B$  ( $= 1,381.10^{-23} \text{J.K}^{-1}$ ) the Boltzmann constant,  $T$  (K) the temperature, and  $k_0$  the prefactor. Above  $C^*$  a good linear fit of equation (3) yields an  $E_a$  value of 0.13eV in the case of electrode A and 0.16eV for K, close to the value for diffusion in the free electrolyte (0.15-0.16eV), [65] while for charge transfer process values of 0.28 and

0.45eV are reported for NMC and LFP, respectively. [87,88] Thus, the temperature dependences of the electrodes time constants  $k_2$  clearly establish that the main limitations of the rate performance is diffusion within the electrolyte into the electrode porosity above  $C^*$ . The activation energy of  $k_1$  was also found equal to 0.28eV in the case of electrode A, suggesting that the rate performance below  $C^*$  is rather dominated by the electrode resistance, itself being affected by the charge transfer process. Discussion about the discharge rate performance of all these electrodes is now divided in two parts, first below  $C^*$  and then above  $C^*$ .

In the case of NMC electrodes (Figure 5a and d), A displays better performance than B, although A has slightly lower mixture conductivity (8.0 vs. 11.8 S.m<sup>-1</sup>) and slightly higher contact resistance (0.08 vs. 0.07 and 0.03Ω.cm<sup>2</sup>). Because B has higher CB+PVdF volume fraction, it can be assumed that the inter-connectivity of NMC with the CB+PVdF mixture is better in B than in A, i.e. higher than 13%. On the other hand, the access of the liquid electrolyte to the NMC particles must be reduced in B compared to A (NMC/electrolyte inter-connectivity value lower than 87%). Thus, below  $C^*$ , the lower rate performance of B is likely due to poorer ionic wiring of the active mass due to the surface covering of the NMC particles by the CB+PVdF phase limiting the liquid electrolyte access and hindering lithium insertion, as shown by the larger polarization and lower capacity. [80,83]

In NMC/LFP electrodes, due to higher amount of CB+PVdF mixture in F (16.4v.%) than in H (11.0v.%), both the NMC and LFP active particles are better contacted to this electronic conducting phase, as seen in the inter-connectivity values (**Figure 3d and e**), 8 and 3% for NMC/CB+PVdF, and 23 and 13% for LFP/CB+PVdF, in F and H, respectively. But, on the other hand, the access to the electrolyte is decreased, from 80 to 77% for NMC and from 86.2 to 76.3% for LFP, in H and F, respectively. **Figure 5b and e,f** clearly show the better performance of F below  $C^*$ . Noteworthy, F and H have nearly the same contact resistance with the current collector, i.e. 1.0 and 0.64 Ω.cm<sup>2</sup>, respectively. Thus the difference in the rate performance can be attributed to improved electronic wiring of the active mass as a consequence of higher inter-connectivity with the CB+PVdF mixture in F. [35] According to M. Gaberscek model,  $R_{\text{electrode}}$  should scale inversely with the inter-connectivity between the active mass and the CB network if the main limitation comes from step (ii), i.e. charge incorporation of both ionic and electronic species. Looking at the voltage profiles (**Figure 5b**) or the capacity delivered by each material ( $Q_{\text{NMC}}$  and  $Q_{\text{LFP}}$ , **Figure 5e,f**), one can see that the drop of capacity in H compared to F is largely due to malfunctioning of NMC. This observation shows that there is a critical NMC/CB+LFP inter-connectivity value for NMC to

well-perform, situated between 3% (F) and 8% (H). Interestingly, G displays nearly similar rate performance than H (**Figure 5b**), although G has a 10 times higher contact resistance with the current collector than H, 7.5 and 0.64Ω.cm<sup>2</sup>, respectively. Such a difference in contact resistance is clearly seen in the higher polarization of G compared to H (**Figure 5b**), especially for the higher C-rates. The same discharge capacity for G and H, which is lower than F, shows however that the inter-connectivity with the CB+PVdF mixture is the governing factor that determines the rate performance up to C\*. The comparison of the behavior of the NMC and LFP materials in the mixed and the unmixed electrodes is delicate matter, in particular because the true current felt by one active matter (in mA per g of NMC or LFP) varies between 1 or 2 times the total current applied to the electrode (in mA per g of NMC+LFP). A comparison of the whole set of electrodes is however feasible above C\* using the discharge front model. [68,71]

Considering that only lithium diffusion limitations determine the rate performance, the degree of discharge (DoD), defined as the capacity discharged at the considered rate, Q<sub>C-rate</sub>, and expressed in percentage of the capacity discharged at low rate, is given by [71]

$$\frac{1}{DoD} = \frac{Q_{C/20}}{Q_{C-rate}} = \frac{L^2 \times (C_{smax,NMC} \times \%v_{NMC} + C_{smax,LFP} \times \%v_{LFP}) \cdot (1-t^+)}{\varepsilon \cdot C_0 \cdot D_{eff}} \cdot \frac{C-rate}{3600} \quad (7)$$

with L (cm) the electrode thickness, C<sub>smax</sub> (mol.cm<sup>-3</sup>) the maximal concentration of inserted species inside the active material, %v<sub>AM</sub> the volumetric fraction of the active material in the electrode, t<sup>+</sup> the cation transport number in the electrolyte (0.41 for Li<sup>+</sup> in LP30 [89]), ε (%) the porosity of the electrode, C<sub>0</sub> the electrolyte concentration (1.10<sup>3</sup>mol.cm<sup>-3</sup>) and D<sub>eff</sub> (cm<sup>2</sup>.s<sup>-1</sup>) the effective diffusion coefficient of the lithium ions through the electrolyte filling the electrode porosity. Equation (7) takes into account the length of the paths the lithium ions must diffuse through the electrode to reach the active mass (depends on L<sup>2</sup>), their kinetics of diffusion (D<sub>eff</sub> that depends through Equations (1) and (2) on D<sub>0</sub>, 2.45.10<sup>6</sup>cm<sup>2</sup>.s<sup>-1</sup> for solvated Li<sup>+</sup> in LP30, [89] ε, α and γ) the mismatch between the maximal concentration of lithium species that could be inserted in the active mass (C<sub>smax</sub>) and the concentration of lithium species in the electrolyte contained in the electrode porosity (C<sub>0</sub>, ε). The maximal concentration of inserted species inside the active material is defined as:

$$C_{smax} = \frac{\rho \cdot \Delta x_{max}}{M} \quad (8)$$

with ρ (g.cm<sup>-3</sup>) the AM density (4.6g.cm<sup>-3</sup> for NMC and 3.6g.cm<sup>-3</sup> for LFP), Δx<sub>max</sub> the maximum reversible insertion degree of the AM (0.61 for NMC and 0.92 for LFP) and M (g.mol<sup>-1</sup>) the AM molecular weight (96.46g.mol<sup>-1</sup> for NMC and 157.76g.mol<sup>-1</sup> for LFP). It gives values of 29.1.10<sup>-3</sup>mol.cm<sup>-3</sup> for NMC and 21.0.10<sup>-3</sup>mol.cm<sup>-3</sup> for LFP.

The discharge capacity at the 2C-rate (thus above  $C^*$ ) predicted by the discharge front model,  $Q_{\text{model}}$ , was calculated with Eq. 7,  $D_{\text{eff}}$  being calculated with Eq. 1 and 2, using mean values of the porosity (**Table 1**), Bruggeman coefficient (determined from tomography measurements,  $\alpha_t$  (**Table 1**), and leaving  $\gamma = 1$ . We considered that the LFP super-calendered K and the as-received J electrodes are characterized by the same Bruggeman coefficient, as this value appears to be characteristic of the spherical shape of the LFP particles. Moreover, both electrodes have same CB+PVdF content. Similarly, we considered that the NMC/LFP electrodes G and H have same Bruggeman coefficients. Measured and calculated values are compared in (**Figure 6a-b**). Very good agreement is found for A (NMC) and F (NMC/LFP) electrodes, which confirms that the discharge front model can be a convenient tool to estimate the rate performance of composite electrodes, as already shown. [68,71] However calculated values are significantly higher than measured ones for G and H (NMC/LFP), J and K (LFP) electrodes. As the model considers only lithium diffusion limitations, the discrepancy observed for G, H, J and K electrodes must root in other limitations among which the electronic wiring limitations (contact resistance, electrical conductivity of the electrode, inter-connectivity with CB+PVdF network). Indeed, J and K have low electronic conductivity values, 0.3 and 0.6 S.m<sup>-1</sup>, respectively, due to lack of CB+PVdF intra-connectivity (25% in J, **Table 1**). Additionally, J has huge contact resistance, 36  $\Omega$ .cm<sup>-2</sup>. G and H have higher electronic conductivity values, 2.4 and 3.4 S.m<sup>-1</sup>, respectively, due to very good CB+PVdF intra-connectivity (92% in H, **Table 1**). However, the poor NMC/CB+PVdF inter-connectivity (3%, **Figure 3d**) negatively affect the rate performance likely because of large polarization, as seen in **Figure 5b**, due to high electrode resistance. Moreover, G has large contact resistance, 7.5  $\Omega$ .cm<sup>-2</sup>, which increases even more the polarization. Comparatively, F has higher electronic conductivity value, 8.0 S.m<sup>-1</sup>, respectively, due to very good CB+PVdF intraconnectivity (92% in H, **Table 1**) and low contact resistance, 1.0  $\Omega$ .cm<sup>-2</sup>. Furthermore, the better NMC/CB+PVdF inter-connectivity (8%, **Figure 3d**) seems to be good enough for this electrode to show only lithium diffusion limitations in power performance. From the architecture and formulation point of view, one can say that in this electrode the electronic wiring of the active mass is fairly well designed. Same conclusion can be drawn for electrode A.

In complement, In **Figure 6c-d** the capacity losses at 2C-rate (expressed in percentage of the discharge capacity measured at very low rate, Eq. 9, or calculated with the discharge front model, Eq. 7) is decomposed into the diffusion and the electronic wiring contributions.

The former considers the drop in capacity that is expected based on the Li<sup>+</sup> diffusion limitation, which is predicted by the discharge front model (Eq. 10).

$$\text{Total losses (\%)} = \frac{Q_{C/20} - Q_{\text{measured}}}{Q_{C/20}} \times 100 \quad (9)$$

$$\text{Diffusion losses (\%)} = \frac{Q_{C/20} - Q_{\text{model}}}{Q_{C/20}} \times 100 \quad (10)$$

The electronic wiring contribution is simply the difference between the total and the diffusion losses. These plots rationalize the efficiency of the different electrode architectures by discriminating the two main types of limitations. Finally, this approach allows comparing the electrode designs. For example, knowing that electrodes A and F show only lithium diffusion limitations in rate performance, one can interpret with relevancy the higher discharge capacity of A compared to F, 100 and 81mAh.g<sup>-1</sup> at 2C-rate, respectively. Looking at the set of equations written above, one can realize that the higher thickness and lower porosity in F detrimentally affect its performance. On the other hand, the performance of A could have been even better with a smaller Bruggeman coefficient. However, its large value is associated with the large size of the NMC particles that form large obstacle to bypass by the ion flux and by the presence of the tortuous CB+PVdF clusters. Interestingly, small capacity loss would be expected for the other electrodes (J, K, G and H) if only there were only lithium diffusion limitations. Their performance is clearly plagued by poor electronic wiring, which emphasizes the critical role of the conductive additive selection and of the electrodes processing to minimize this limitation. Same trends are observed at 3C-rate (**Figure S11**), but the contribution of the lithium diffusion limitations becomes more important.

### 3. Conclusion

Combination of X-ray and FIB-SEM tomography techniques with BDS, together with the use of the electrochemical discharge front model, allow establishing unambiguous relationships between electrode 3D geometry, electrical properties and electrochemical performance. Moreover, quantitative assessment of the contributions of the electronic and ionic wiring limitations to power performance is achieved for the first time. Below a critical regime C\*, between 1C and 1.5C, the discharge capacity depends on the electrode resistance that is determined by the contact resistance at the electrode/collector interface, the percolation of the CB+PVdF mixture, the contact surface area between the active particles and this mixture, and also with the electrolyte. Above C\*, for electrodes with suitable electronic wiring, the discharge capacity is determined by the limitations opposed to lithium diffusion into the electrode pores tortuosity. The latter contribution can be satisfactorily estimated by

using the discharge front model and a Bruggeman coefficient calculated from the product of the micro- and nano-scale geometrical tortuosity factors. The large NMC particle size, compared to the pores and/or LFP particles, favors the CB+PVdF mixture percolation but also higher pores tortuosity. The small LFP particles disfavor CB+PVdF percolation but favor lower pores tortuosity.

For LFP electrode at 3wt% of CB, the CB+PVdF mixture does not percolate as it is scattered among LFP particles, which results in very poor rate performance. Contrarily, in NMC electrode, the CB+PVdF mixture percolates and contacts 13% of the NMC particles surface area, leaving 87% of it accessible to the liquid electrolyte. It results low electrode resistance below  $C^*$  and rate performance mostly determined above  $C^*$  by the limitations opposed to lithium diffusion into the electrode pores tortuosity. Increasing at 4.5wt% the CB content allows the CB+PVdF mixture percolation in LFP electrode, reaching a target value of more than  $3S.m^{-1}$  for  $\sigma_{dc}$ , which restores satisfactory rate performance below and above  $C^*$ . Contrarily, rate performance is degraded in NMC electrode as a consequence of insufficient access of the liquid electrolyte to the surface of NMC particles, which slows down the charge transfer process.

In NMC/LFP electrode, at 3wt% of CB, the CB+PVdF mixture percolates, despite its scattering among LFP particles, because of higher CB+PVdF to LFP ratio than in LFP electrode with same CB content. However, NMC particles are starved from electrons as less than 3% of their surface area is contacted by the CB+PVdF mixture. It results poor rate performance. Increasing CB content at 4.5wt% allows retrieving enough electronic wiring of the NMC particles, 8% of their surface area being contacted by the CB+PVdF mixture, and also better electronic wiring of the LFP ones. It results low electrode resistance and rate performance above  $C^*$  mostly determined by the limitations opposed to lithium diffusion into the electrode pores tortuosity. Then, a value between 3 and 8% of NMC inter-connectivity with CB+PVdF can be targeted for optimum charge transfer process.

The measurement by BDS of the contact resistance at the electrode/collector interface showed the influence of this parameter and of calendaring on electrochemical performance. Discussing only electrodes with percolation of the CB+PVdF mixture, insufficient calendaring can lead to high contact resistance with significant effect on electrode polarization, as a consequence of low areal density of contact points. A value of  $1\text{ Ohm.cm}^{-2}$  can be targeted for negligible influence of the contact resistance on electrochemical performance.

All these results are relevant for battery technology because they were obtained for electrodes relevant for the industry in terms of composition, surface capacity, and manufacturing process. This work opens new prospects for rational electrode design, which is critical to build higher energy and power density batteries, in particular of EV application. Searching for critical inter-connectivity values between the active particles and the electronic and ionic networks, as a function of materials parameters (particles intrinsic conductivity, size and shape) to achieve low electrode resistance looks very interesting.

#### **4. Experimental section**

Experimental section is given in Supporting Information (SI) due to space limitation.

#### **Supporting Information**

Supporting Information is available from the Wiley Online Library or from the author.

#### **Acknowledgements**

Financial funding from the ANR program no. ANR-15-CE05-0001-01 is acknowledged. The authors would like to acknowledge IMD (Institut de la Mobilité Durable – Sustainable Mobility Institute) and the network METSA (Microscopie Electronique et Sonde Atomique) for financial support. Thanks are also due to the CLYM (Centre Lyonnais de Microscopie: [www.clym.fr](http://www.clym.fr)) supported by the CNRS, the "Grand Lyon" and the Rhône-Alpes Region for use of the Zeiss NVision40 FIB/SEM. This work was made possible by the facilities provided by Swiss Light Sources (Paul Scherrer Institut) and the technical support from the staff of the TOMCAT beamline.

Received: ((will be filled in by the editorial staff))

Revised: ((will be filled in by the editorial staff))

Published online: ((will be filled in by the editorial staff))

**Table captions**

**Table 1** Composition, porosity and thickness (without aluminum collector) of NMC, LFP and blended NMC/LFP electrodes. Morphological parameters evaluated from X-Ray and FIB/SEM tomography reconstructions and electrical properties measured by Broadband Dielectric Spectroscopy. All electrodes have a loading of  $2.6 \text{ mAh.cm}^{-2}$ , except J', K' and L' ( $1.8 \text{ mAh.cm}^{-2}$ ). "n.m." means "not-measured"

**Figure captions**

**Figure 1** 2D and 3D FIB/SEM reconstructed views of (a-b) A (NMC), (c-d) F (NMC/LFP), (e-f) H (NMC/LFP) and (g-h) J (LFP) electrodes. NMC particles are red, LFP particles are green, the CB+PVdF mixture is blue and the porosity is white.

**Figure 2** 3D FIB/SEM reconstructed views of the NMC particles with the NMC surface area in contact with LFP (green zone), CB+PVdF mixture (blue zone) and porosity (grey zone) for (a) A (NMC), (b) F (NMC/LFP) and (c) H (NMC/LFP). Interconnectivity between the different materials/phases given as the specific surface area of (d) NMC, (e) LFP and (f) CB+PVdF mixture in contact with the other materials/phases for electrodes A, F, H and J.

**Figure 3** (a) Pore size distribution; (b) Tortuosity factor through electrodes thickness (y-direction); 2D pores tortuosity factor  $T_v$  representation for (c) A (NMC), (d) F (NMC/LFP), (e) H (NMC/LFP) and (f) J (LFP) electrodes. The side close to the electrode surface is in all cases at the bottom of the 2D maps.

**Figure 4** Real part of the complex conductivity as function of the frequency for (a) A (NMC) and F, G, and H (NMC/LFP); and (b) J, K, and L (LFP) electrodes. (c) Contact resistance and electrode conductivity; and (d) calculated value of areal density of contacts at the electrode/current collector interface for K, G, H and A.

**Figure 5** Potential vs. specific capacity curves at three C-rates ( $C/20$ ,  $C$  and  $2C$ ) for (a) A, B (NMC); (b) F, G, and H (NMC/LFP); (c) J, K (LFP) electrodes. Discharge capacity as function of the C-rate for (a) A, B (NMC) and J, K (LFP); (e) F (NMC/LFP); (f) H (NMC/LFP) electrodes. The arrows mark the critical discharge rate,  $C^*$ . For NMC/LFP electrodes, the capacity delivered by each active material is also plotted in (e) and (f).

**Figure 6** Comparison between the measured and calculated (Eq. 7) discharge capacity at  $2C$ -rate for (a) A (NMC), J and K (LFP); (b) F, G and H (NMC/LFP) electrodes. Capacity loss at  $2C$ -rate (Eq. 9-10) decomposed into the diffusion and electronic wiring contributions for (c) A (NMC), J and K (LFP); (d) F, G and H (NMC/LFP) electrodes.

Table 1

	NMC/LFP Compaction	Content (w.%)/(v%)	Porosity (vol. %)	Thickness ( $\mu\text{m}$ )	Intra- connectivity (%)	Tortuosity factors and Bruggeman coefficient	Electrical Properties: contact resistance, areal density of contact points, electrode conductivity (electrode and eventually isolated CB+PVdF clusters), activation energy	
							$R_C$ ( $\Omega\cdot\text{cm}^2$ ) $\Sigma$ (a.u.)	$\sigma_{dc}$ (S/m) – $E_a$ (eV) $\sigma_{\text{isolated CB+PVdF}}$ (S/m) – $E_a$ (eV)
		NMC LFP PVdF CB		Micrometer XCT	NMC LFP CB+PVdF Pores	$T_o$ (micro) $T_u$ (nano) $\alpha_t$		
A	100/0 As-received	92/54.2 0 5/7.6 3/4.2	34	69 73	99.8 - 77 100	1.22 2.10 1.54	0.08  152	8.0 – ~0
B	100/0 As-received	88/52.2 0 7.5/11.5 4.5/6.3	30	73 81	99.4 n.m. n.m. n.m.	1.14 n.m. n.m.	0.07  139	10.7 – n.m.
F	50/50 As-received	44/24.0 44/30.6 7.5/10.6 4.5/5.8	29	77 78	13.6 100 88 100	1.06 1.38 1.34	1.0  12	8.1 – n.m.
G	50/50 As-received	46/24.0 46/30.6 5/6.7 3/3.7	35	77 77	15.0 n.m. n.m. n.m.	1.06 n.m. n.m.	7.5  5.6	2.4 – n.m. 8.1 – n.m.
H	50/50 Super calendered	46/25.5 46/32.5 5/7.1 3/3.9	31	71 73	16.3 100 92 100	1.06 1.42 1.30	0.64  45	3.4 – n.m.
J	0/100 As-received	0 92/53.9 5/5.9 3/3.2	37	88 95	- 100 25 100	1.00 1.25 1.20	36.6  9	0.3 – 0.07 4.1 – ~0
J'	0/100 As-received	0 92/53.9 5/5.9 3/3.2	37	61 n.m.	- n.m. n.m. n.m.	1.00 n.m. n.m.	3.8  61	0.4 – n.m. 5.3 – n.m.
K	0/100 Super calendered	0 92/59.8 5/6.6 3/3.6	30	78 80	- n.m. n.m. n.m.	1.00 n.m. n.m.	0.8  208	0.6 – 0.06 6.3 – ~0
K'	0/100 Super calendered	0 92/59.8 5/6.6 3/3.6	30	57 n.m.	- n.m. n.m. n.m.	1.00 n.m. n.m.	0.4  369	0.7 – n.m. 7.8 – n.m.
L'	0/100 Super calendered	0 88/54.5 7.5/9.4 4.5/5.1	31	59 n.m.	- n.m. n.m. n.m.	1.00 n.m. n.m.	0.29  107	3.3 – n.m.

## References

- <sup>1</sup> M. Winter, R.J. Brodd, *Chem. Rev.* **2004**, *104*, 4245
- <sup>2</sup> E. J. Berg, C. Villevieille, D. Streich, S. Trabesinger, P. Novák, *J. Electrochem. Soc.* **2015**, *162*, A2468
- <sup>3</sup> J. W. Choi, D. Aurbach, *Nature Rev. Mater.* **2016**, *1*, 1
- <sup>4</sup> J.S. Wang, P. Liu, E. Sherman, M. Verbrugge, H. Tataria, *J. Power Sources.* **2011**, *196*, 8714
- <sup>5</sup> S.J. Dillon, K. Sun, *Current Opinion Solid State Mater. Sci.*, **2012**, *16*, 153.
- <sup>6</sup> K. Evanoff, J. Khan, A. A. Balandin, A. Magasinski, W. J. Ready, T. F. Fuller, G. Yushin, *Adv. Mater.*, **2012**, *24*, 533
- <sup>7</sup> H. Munakata, B. Takemura, T. Saito, K. Kanamura, *J. Power Sources*, **2012**, *217*, 444

- <sup>8</sup> S.-L. Wu, W. Zhang, X. Song, A.K. Shukla, G. Liu, V. Battaglia, V. Srinivasan, *J. Electrochem. Soc.*, **2012**, *159*, A438
- <sup>9</sup> J. Billaud, F. Bouville, T. Magrini, C. Villevieille, A.R. Studart, *Nature Energy*, doi: 10.1038/nenergy.2016.97
- <sup>10</sup> V. Srinivasan, J. Newman, *J. Electrochem. Soc.*, **2004**, *151*, A1517
- <sup>11</sup> J. Liu, M. Kunz, K. Chen, N. Tamura, T.J. Richardson, *J. Phys. Chem. Lett.*, **2010**, *1*, 2120
- <sup>12</sup> D. Robert, T. Douillard, A. Boulineau, G. Brunetti, P. Nowakowski, D. Venet, P. Bayle-Guillemaud, C. Cayron, *ACS Nano*, **2013**, *7*, 10887
- <sup>13</sup> M. Katayama, K. Sumiwakaa, R. Miyaharaa, H. Yamashige, H. Arai, Y. Uchimoto, T. Ohta, Y. Inada, Z. Ogumi, *J. Power Sources*, **2014**, *269*, 994
- <sup>14</sup> G. Ouvrard, M. Zerrouki, P. Soudan, B. Lestriez, C. Masquelier, M. Morcrette, S. Hamelet, J. Lesage, S. Belin, A.M Flank, F. Baudelet, *J. Power Sources*, **2013**, *229*, 16
- <sup>15</sup> D.M. Robert, A. Madsen, C. Nicklin, J. Rawle, M. G. Palmer, J.R. Owen, A.L. Hector, *J. Phys. Chem. C*, **2014**, *118*, 6548
- <sup>16</sup> X. Zhang, T.W. Verhallen, F. Labohm, M. Wagemaker, *Adv. Energy Mater.*, **2015**, *5*, 1500498
- <sup>17</sup> P.R. Shearing, L.E. Howard, P.S. Jørgensen, N.P. Brandon, S.J. Harris, *Electrochem. Commun.*, **2010**, *12*, 374
- <sup>18</sup> P.R. Shearing, N.P. Brandon, J. Gelb, R. Bradley, P.J. Withers, A.J. Marquis, S. Cooper, S.J. Harris, *J. Electrochem. Soc.*, **2012**, *159*, A1023
- <sup>19</sup> M. Ebner, F. Geldmacher, F. Marone, M. Stampanoni, V. Wood, *Adv. Energy Mater.* **2013**, *3*, 845
- <sup>20</sup> Y.-C.K. Chen-Wiegart, Z. Liu, K.T. Faber, S.A. Barnett, J. Wang, *Electrochem. Comm.* **2013**, *28*, 127
- <sup>21</sup> M. Ender, J. Joos, A. Weber, E. Ivers-Tiffée, *J. Power Sources*, **2014**, *269*, 912
- <sup>22</sup> Y.-C.K. Chen-Wiegart, R. DeMike, C. Erdonmez, K. Thornton, S.A. Barnett, J. Wang, *J. Power Sources*, **2014**, *249*, 349
- <sup>23</sup> Y.-C.K. Chen-Wiegart, R. DeMike, C. Erdonmez, K. Thornton, S.A. Barnett, J. Wang, *J. Power Sources*, **2014**, *249*, 349
- <sup>24</sup> M. Ebner, D.-W. Chung, R. E. García, and V. Wood, *Adv Energy Mater.* **2014**, *4*, 1301278
- <sup>25</sup> F. Tarik, V. Yufit, M. Kishimoto, P.R. Shearing, S. Menkin, D. Golodnitsky, J. Gelb, E. Peled, N.P. Brandon, *J. Power Sources*, **2014**, *248*, 1014
- <sup>26</sup> S. K. Babu, A. Mohamed, J. Whitacre, *J. Power Sources*, **2015**, *283*, 314
- <sup>27</sup> J.R. Wilson, S. A. Barnett, J. S. Cronin, and S. J. Harris, *J. Power Sources* **2011**, *196*, 3443
- <sup>28</sup> a) M. Ender, J. Joos, T. Carraro, E. Ivers-Tiffée, *Electrochem. Comm.*, **2011**, *13*, 166. b) M. Ender, J. Joos, T. Carraro, E. Ivers-Tiffée, *J. Electrochem. Soc.* **2012**, *159*, A972
- <sup>29</sup> T. Hutzenlaub, S. Thiele, R. Zengerle, C. Ziegler, *Electrochem. Solid-State Lett.* **2012**, *15*, A33
- <sup>30</sup> T. Hutzenlaub, A. Asthana, J. Becker, D.R. Wheeler, R. Zengerle, S. Thiele, *Electrochem. Comm.* **2013**, *27*, 77
- <sup>31</sup> S. Vierrath, L. Zielke, R. Moroni, A. Mondon, D.R. Wheeler, R. Zengerle, S. Thiele. *Electrochem. Commun.*, **2015**, *60*, 176
- <sup>32</sup> Z. Liu, J.S. Cronin, Y.-C.K. Chen-Wiegart, J.R. Wilson, K.J. Yakal-Kremiski, J. Wang, K.T. Faber, S.A. Barnett, *J. Power Sources*, **2013**, *227*, 267
- <sup>33</sup> a) L. Zielke, T. Hutzenlaub, D. R. Wheeler, I. Manke, T. Arlt, N. Paust, R. Zengerle, S. Thiele, *Adv. Energy Mater.*, **2014**, *13*, 1617. b) L. Zielke, T. Hutzenlaub, D.R. Wheeler, C.-W. Chao, I. Manke, A. Hilger, N. Paust, R. Zengerle, S. Thiele, *Adv. Energy Mater.*, **2015**, *5*, 1401612
- <sup>34</sup> D. Kehrwald, P.R. Shearing, N.P. Brandon, P.K. Sinha, S.J. Harris, *J. Electrochem. Soc.*, **2011**, *158*, A1393

- <sup>35</sup> H. Liu, J.M. Foster, A. Gully, S. Krachkovskiy, M. Jiang, Y. Wu, X. Yang, B. Protas, G.R. Goward, G.A. Botton, *J. Power Sources*, **2016**, 306, 300
- <sup>36</sup> D.E. Stephenson, B.C. Walker, C.B. Skelton, E.P. Gorzkowski, D.J. Rowenhorst, D.R. Wheeler, *J. Electrochem Soc.*, **2011**, 158, A781
- <sup>37</sup> B. Yan, C. Lim, L. Yin, L. Zhu, *J. Electrochem. Soc.*, **2012**, 159, A1604
- <sup>38</sup> A.H. Wiedemann, G.M. Goldin, S.A. Barnett, H. Zhu, R.J. Kee, *Electrochim. Acta*, **2013**, 88, 580
- <sup>39</sup> T. Hutzenlaub, S. Thiele, N. Paust, R. Spotnitz, R. Zengerle, C. Walchshofer, *Electrochim. Acta*, **2014**, 115, 131
- <sup>40</sup> A.G. Kashkooli, S. Farhad, D.U. Lee, K. Feng, S. Litster, S.K. Babu, L. Zhu, Z. Chen, *J. Power Sources*, **2016**, 307, 496
- <sup>41</sup> S.B. Chikkannanavar, D.M. Bernardi, L. Liu, *J. Power Sources*, **2014**, 248, 91
- <sup>42</sup> L. Liu, X. Yan, Y. Wang, D. Zhang, F. Du, C. Wang, G. Chen, Y. Wei, *Ionics*, **2014**, 20, 1087
- <sup>43</sup> N. Imachi, Y. Takano, H. Fujimoto, Y. Kida, S. Fujitani, *J. Electrochem. Soc.*, **2007**, 154, A412.
- <sup>44</sup> J.F. Whitacre, K. Zaghbi, W.C. West, B.V. Ratnakumar, *J Power Sources*, **2008**, 177, 528
- <sup>45</sup> W. Haselrieder, S. Ivanov, H.Y. Tran, S. Theil, L. Froböse, B. Westphal, M. Wohlfahrt-Mehrens, A. Kwade, *Progress in Solid State Chemistry*, **2014**, 42, 157
- <sup>46</sup> E. Maire, O.J. Withers, *Int. Mater. Rev.*, **2014**, 59, 1
- <sup>47</sup> A. Etienne, N. Besnard, J. Adrien, P. Tran-Van, L. Gautier, B. Lestriez, E. Maire, *J. Power Sources*, **2015**, 298, 285
- <sup>48</sup> A. Etienne, N. Besnard, A. Bonnin, J. Adrien, T. Douillard, P. Tran-Van, L. Gautier, J.-C. Badot, E. Maire, B. Lestriez, *J. Mater. Sci.*, **2016**, doi:10.1007/s10853-016-0374-x
- <sup>49</sup> Da, H. and N.N. Ekere, *J. Phys. D: Appl. Phys.*, **2004**, 37, 1848
- <sup>50</sup> a) Yoo, M., C.W. Frank, S. Mori, *Chem. Mater.*, **2003**, 15, 850. b) Yoo, M., C.W. Frank, S. Mori, S. Yamaguchi, *Chem. Mater.*, **2004**, 16, 1945
- <sup>51</sup> K.C. Kil, M.E. Lee, G.Y. Kim, C.-W. Cho, K. Kim, G. Kim, U. Paik, *J. Phys. Chem. C*, **2011**, 115, 16242
- <sup>52</sup> T. DuBeshter, P.K. Sinha, A. Sakars, G.W. Fly, J. Jorne, *J. Electrochem.Soc.*, **2014**, 161, A599
- <sup>53</sup> a) N.A. Zacharias, D.R. Nevers, C. Skelton, K. Knackstedt, D.E., Stephenson, D.R. Wheeler, *J. Electrochem. Soc.*, **2013**, 160, A306. b) I.V. Thorat, D.E. Stephenson, N.A. Zacharias, K. Zaghbi, J.N. Harb, D.R. Wheeler, *J. Power Sources*, **2009**, 188, 592
- <sup>54</sup> M. Loretz, E. Maire, D. Baillis, *Adv. Eng. Mater.*, **2008**, 10, 352
- <sup>55</sup> a) Vijayaraghavan, D.R. Ely, Y.-M. Chiang, R. García-García, R.E. García, *J. Electrochem. Soc.*, **2012**, 159, A548. b) D.-W., Chung, M. Ebner, D.R. Ely, V. Wood, R.E. García, *Modelling Simul. Mater. Sci. Eng.*, **2013**, 21, 074009
- <sup>56</sup> A. Morales-Rodríguez, P. Reynaud, G. Fantozzi, J. Adrien, E. Maire, *Scripta Materialia*, **2009**, 60, 388
- <sup>57</sup> Y.-C.K. Chen-Wiegart, T. Wada, N. Butakov, X. Xiao, F. De Carlo, H. Kato, J. Wang, D.C. Dunand, E. Maire, *J. Mater. Research*, **2013**, 28, 2444
- <sup>58</sup> a) J-C. Badot, E. Ligneel, O. Dubrunfaut, D. Guyomard, B. Lestriez, *Adv. Funct. Mater.*, **2009**, 19, 2749. b) J-C. Badot, E. Ligneel, O. Dubrunfaut, J. Gaubicher, D. Guyomard, B. Lestriez, *Phys. Chem. Chem. Phys.*, **2012**, 14, 9500
- <sup>59</sup> K.A. Seid, J.C. Badot, O. Dubrunfaut, M.T. Caldes, N. Stephant, L. Gautier, D. Guyomard and B. Lestriez, *Phys. Chem. Chem. Phys.*, **2013**, 15, 19790
- <sup>60</sup> a) K.A. Seid, J-C. Badot, O. Dubrunfaut, S. Levasseur, D. Guyomard, B. Lestriez, *J. Mater. Chem.*, **2012**, 22, 2641. b) K.A. Seid, J-C. Badot, O. Dubrunfaut, S. Levasseur, D. Guyomard, B. Lestriez, *J. Mater. Chem.*, 2012, 22, 24057

- <sup>61</sup> J.-C. Badot, B. Lestriez, O. Dubrunfaut, *Mater. Sci. Eng.*, **2016**, doi:10.1016/j.mseb.2016.05.012
- <sup>62</sup> A. Awarke, M. Wittler, S. Pischinger, J. Bockstette, *J. Electrochem. Soc.*, **2012**, *159*, A798
- <sup>63</sup> A. van Bommel, R. Divigalpitiya, *J. Electrochem. Soc.*, **2012**, *159*, A1791
- <sup>64</sup> J.-H. Hwang, K.S. Kirkpatrick, T.O. Mason, E.J. Garboczi, *Solid State Ionics*, **1997**, *98*, 93
- <sup>65</sup> K-A. Seid, J-C. Badot, C. Perca, O. Dubrunfaut, P. Soudan, D. Guyomard, B. Lestriez., *Adv. Energy Mater.*, **2015**, *5*, 1400903
- <sup>66</sup> H. Zheng, J. Li, X. Song, G. Liu, V.S. Battaglia, *Electrochim Acta*, **2012**, *71*, 258
- <sup>67</sup> D.Y.W. Yu, K. Donoue, T. Inoue, M. Fujimoto, S. Fujitani, *J. Electrochem. Soc.*, **2006**, *53*, A835
- <sup>68</sup> A. Johns, M.R. Roberts, Y. Wakizaka, J.H. Sanders, J.R. Owen, *Electrochem. Commun.*, **2009**, *11*, 2089
- <sup>69</sup> a) C. Fongy, A.C. Gaillot, S. Jouanneau, D. Guyomard, B. Lestriez, *J. Electrochem. Soc.*, **2010**, *157*, A885. b) C. Fongy, S. Jouanneau, D. Guyomard, J-C. Badot, B. Lestriez, *J. Electrochem. Soc.*, **2010**, *157*, A1347
- <sup>70</sup> D.P. Singh, F.M. Mulder, A.M. Abdelkader, M. Wagemaker, *Adv. Energy Mater.*, **2013**, *3*, 572
- <sup>71</sup> R. Cornut, D. Lepage, S.B. Schougaard, *Electrochim. Acta*, **2015**, *162*, 271
- <sup>72</sup> Y. Orikasa, Y. Gogyo, H. Yamashige, M. Katayama, K. Chen, T. Mori, K. Yamamoto, T. Masese, Y. Inada, T. Ohta, Z. Siroma, S. Kato, H. Kinoshita, H. Arai, Z. Ogumi, Y. Uchimoto, *Sci. Rep.*, **2016**, *6*, 26382; doi: 10.1038/srep26382
- <sup>73</sup> M. Gaberscek, *J. Power Sources*, **2009**, *189*, 22
- <sup>74</sup> N. Ogihara, Y. Itou, T. Sasaki, Y. Takeuchi, *J. Phys. Chem. C*, **2015**, *119*, 4612
- <sup>75</sup> a) M. Gaberscek, J. Moskon, B. Erjavec, R. Dominko, J. Jamnik, *Electrochem. Solid-State Lett.*, **2008**, *11*, A170. b) J.-M. Atebamba, J. Moskon, S. Pejovnik, M. Gaberscek, *J. Electrochem. Soc.*, **2010**, *157*, A1218
- <sup>76</sup> a) M. Gaberscek, M. Bele, J. Drogenik, R. Dominko and S. Pejovnik, *Electrochem. Solid-State Lett.*, **2000**, *3*, 171. b) R. Dominko, M. Gaberscek, J. Drogenik, M. Bele and S. Pejovnik, *Electrochem. Solid-State Lett.*, **2001**, *4*, A187. c) R. Dominko, M. Gaberscek, J. Drogenik, M. Bele, S. Pejovnik and J. Jamnik, *J. Power Sources*, **2003**, *119–121*, 770
- <sup>77</sup> D. Guy, B. Lestriez, R. Bouchet, D. Guyomard, *J. Electrochem. Soc.*, **2006**, *153*, A679
- <sup>78</sup> M. Gaberscek, J. Jamnik, *Solid State Ionics*, **2006**, *177*, 2647
- <sup>79</sup> R. Cornut, D. Lepage, S.B. Schougaard, *J. Electrochem. Soc.*, **2012**, *159*, A822
- <sup>80</sup> G. Liu, H. Zheng, S. Kim, Y. Deng, A. M. Minor, X. Song, V. S. Battaglia, *J. Electrochem. Soc.*, **2008**, *155*, A887
- <sup>81</sup> E. Ligneel, B. Lestriez, A. Hudhomme, D. Guyomard, *Electrochem. Solid-State Lett.*, **2007**, *10*, A122
- <sup>82</sup> M. Kaneko, M. Nakayama, M. Wakihara, *J. Solid State Electrochem.*, **2007**, *11*, 1071
- <sup>83</sup> H. Zheng, G. Liu, X. Song, P. Ridgway, S. Xun, V.S. Battaglia, *J. Electrochem. Soc.*, **2010**, *157*, A1060
- <sup>84</sup> P.P. Prosini, *J. Electrochem. Soc.*, **2005**, *152*, A1925
- <sup>85</sup> S. Yu, Y. Chung, M.S. Song, J.H. Nam, W.I. Cho, *J. Appl. Electrochem.*, **2012**, *42*, 443
- <sup>86</sup> M. Okubo, Y. Tanaka, H. Zhou, T. Kudo, I. Honma, *J. Phys. Chem. B*, **2009**, *113*, 2840
- <sup>87</sup> J. Xu, S.-L. Chou, Q.-f. Gu, H.-K. Liu, S.-X. Dou, *J. Power Sources*, **2013**, *225*, 172
- <sup>88</sup> J. Illig, M. Ender, T. Chrobak, J. P. Schmidt, D. Klotz and E. Ivers-Tiffée, *J. Electrochem. Soc.*, **2012**, *159*, A952
- <sup>89</sup> L. Niedzicki, S. Grugeon, S. Laruelle, P. Judeinstein, M. Bukowska, J. Prejzner, P. Szczecinski, W. Wieczorek, M. Armand, *J. Power Sources*, **2011**, *196*, 8696

Figure 1

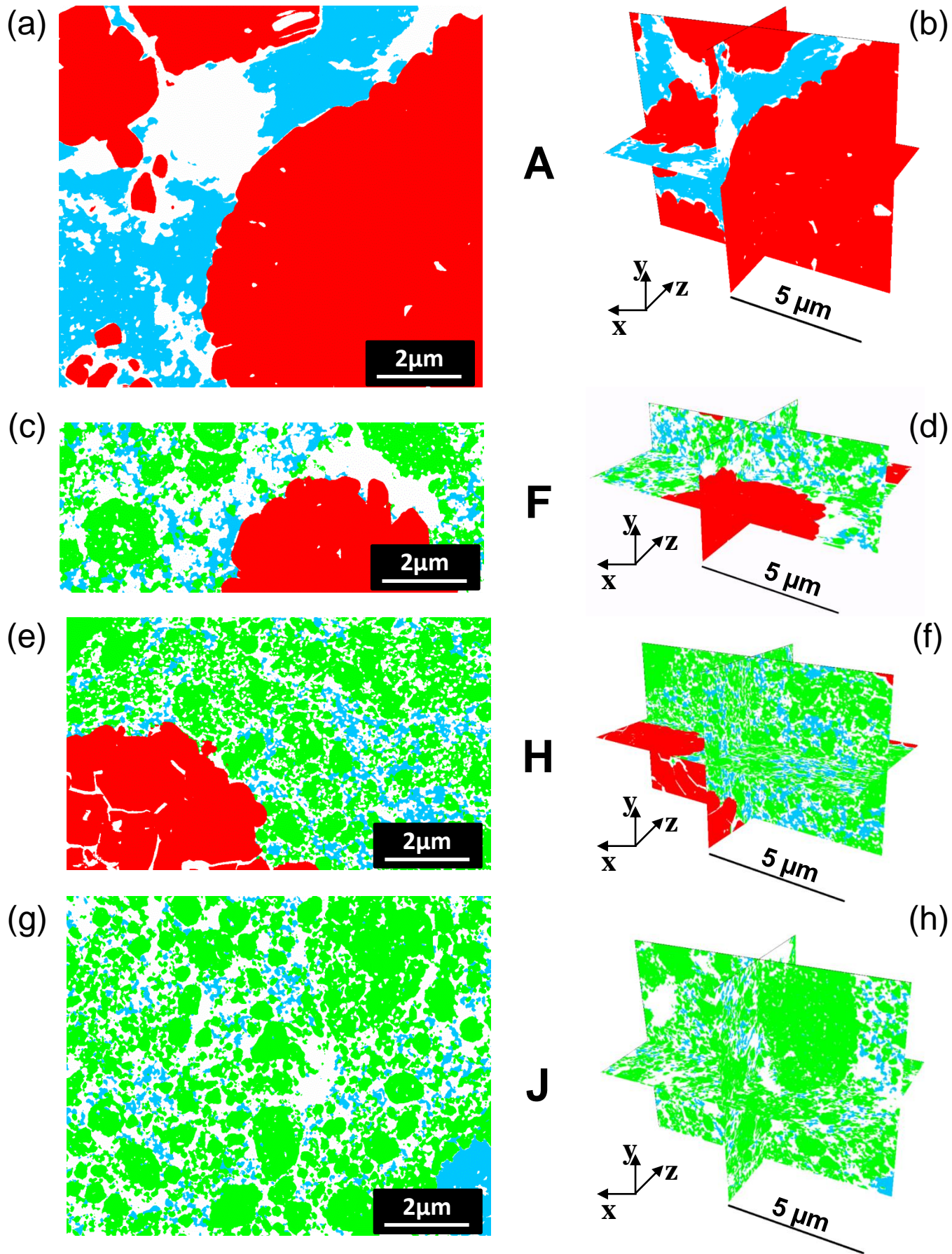
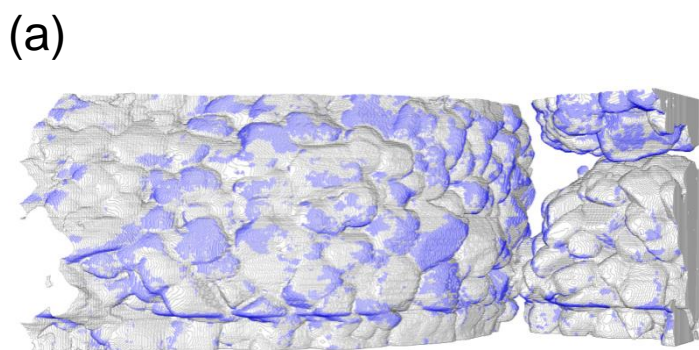
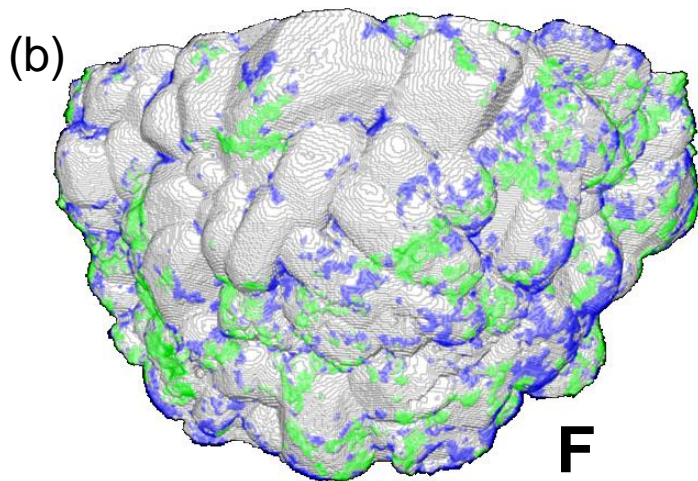


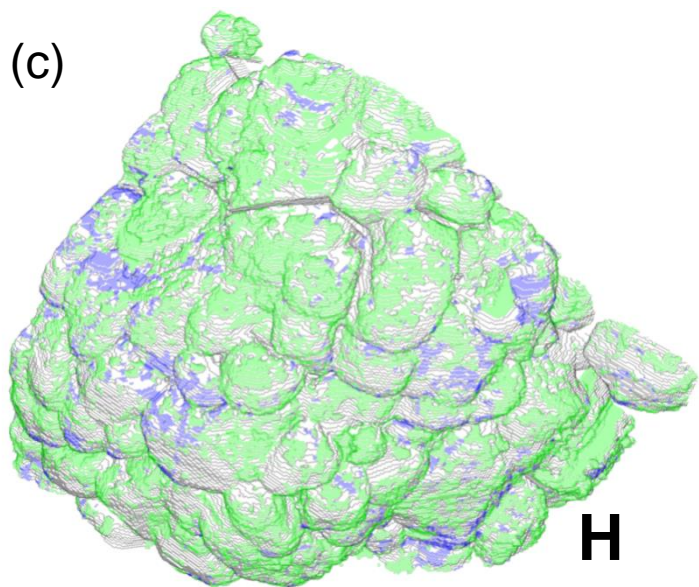
Figure 2



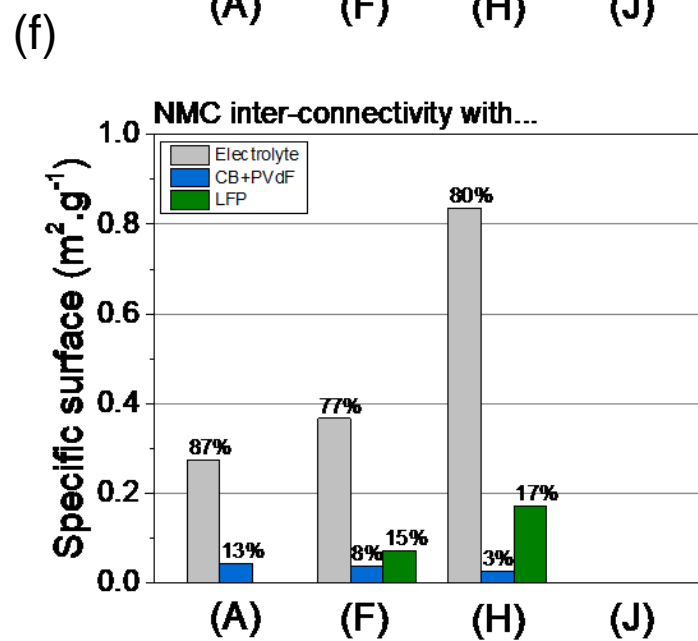
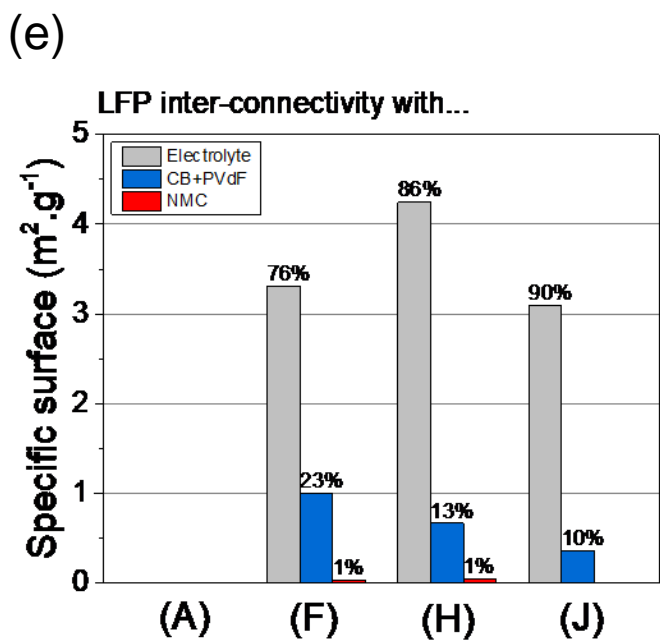
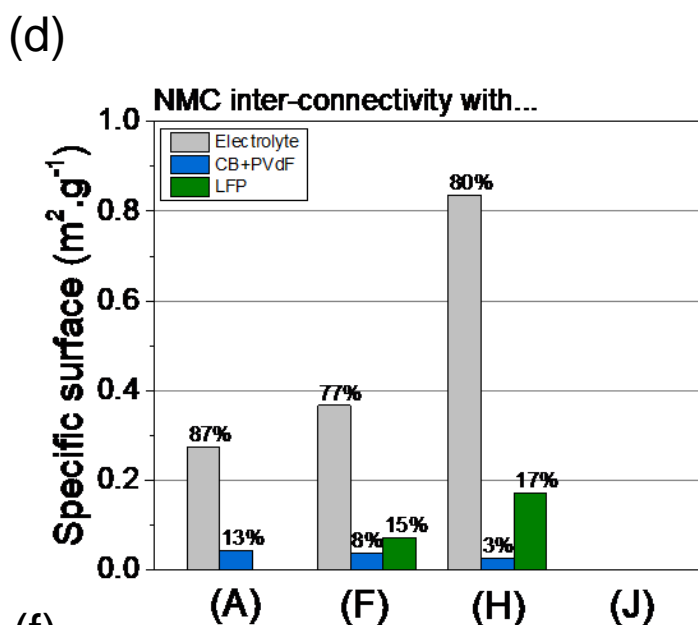
**A**



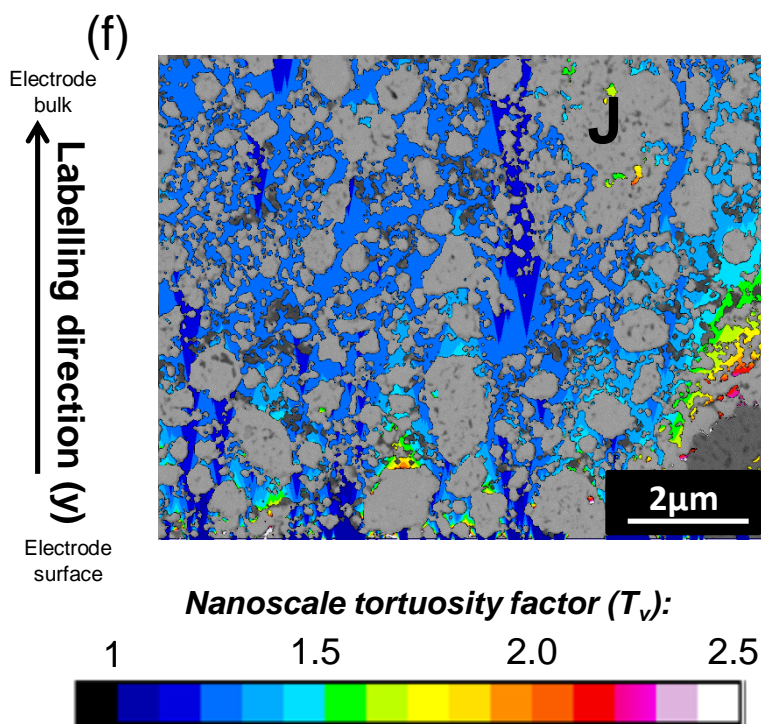
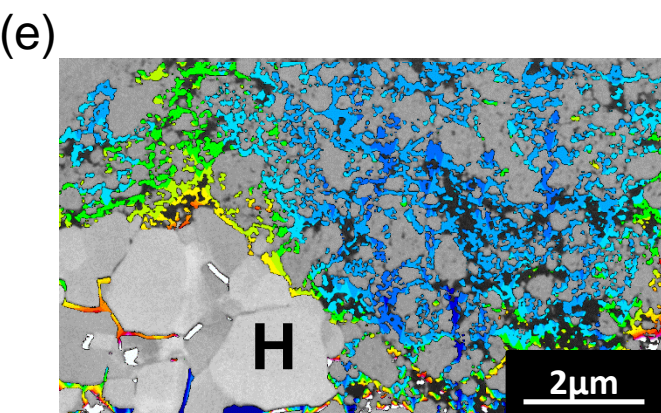
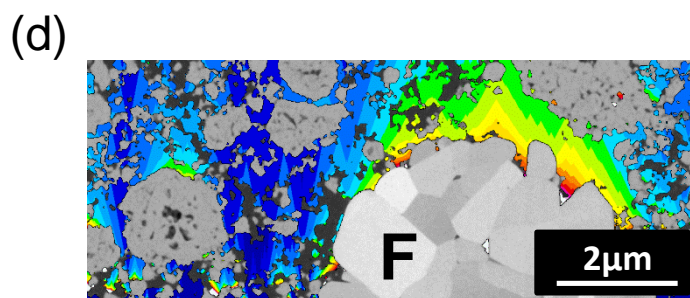
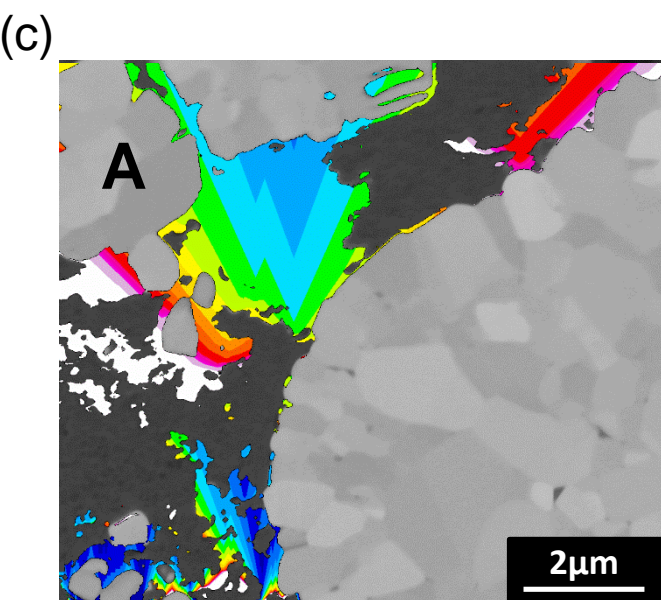
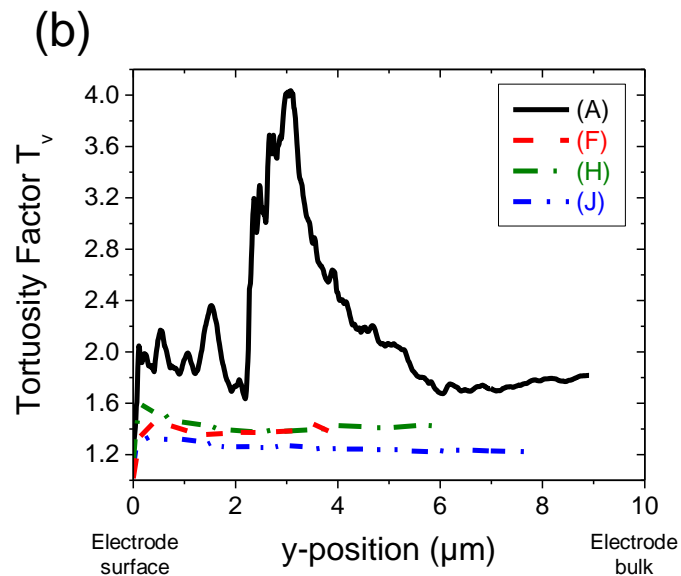
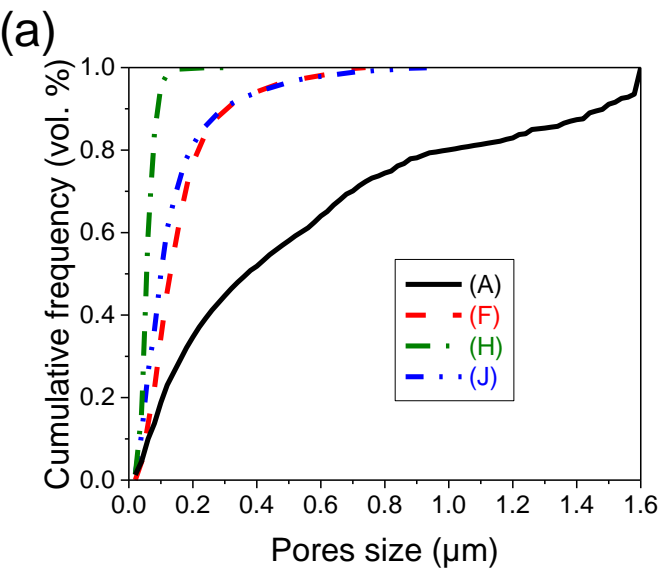
**F**

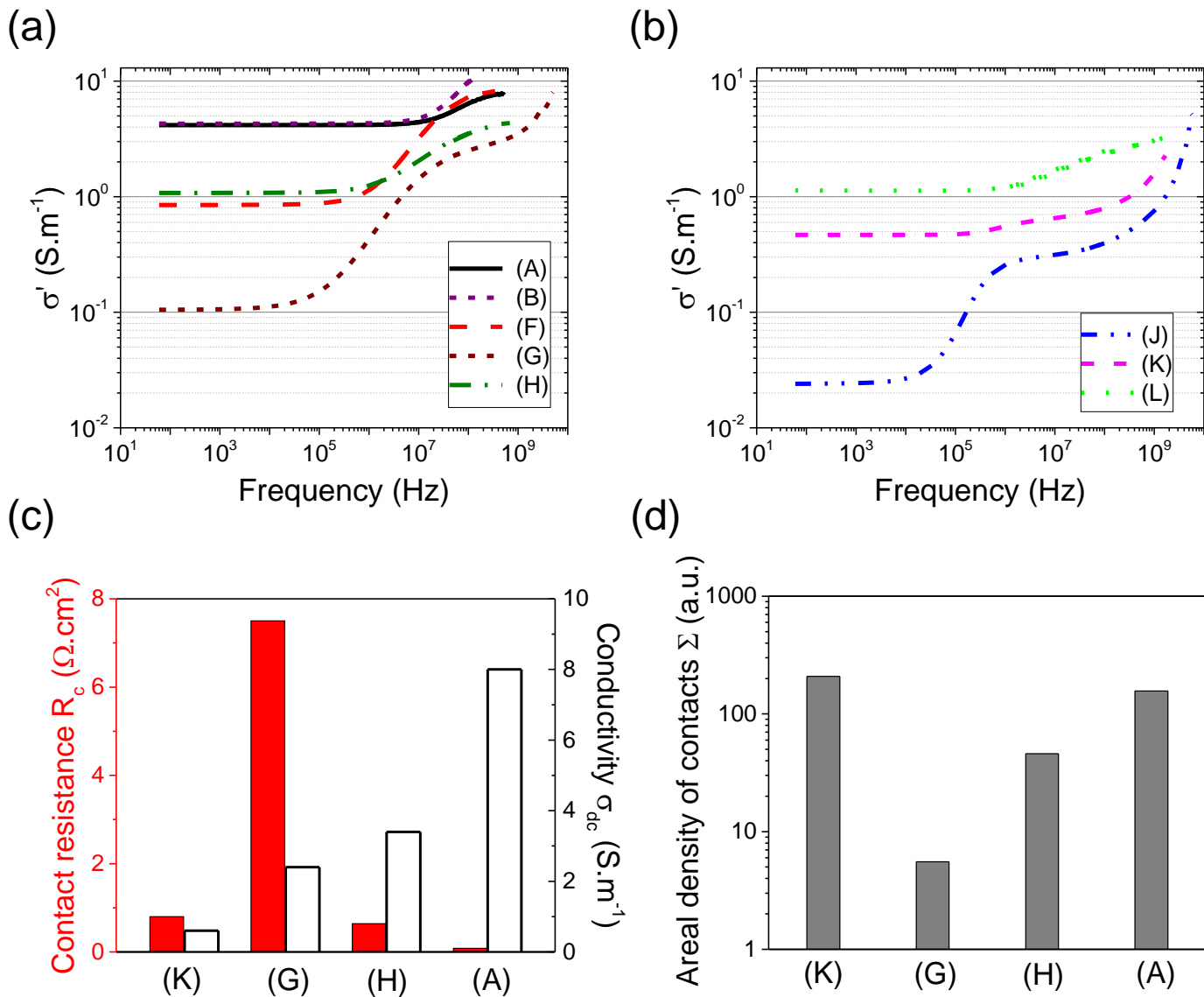


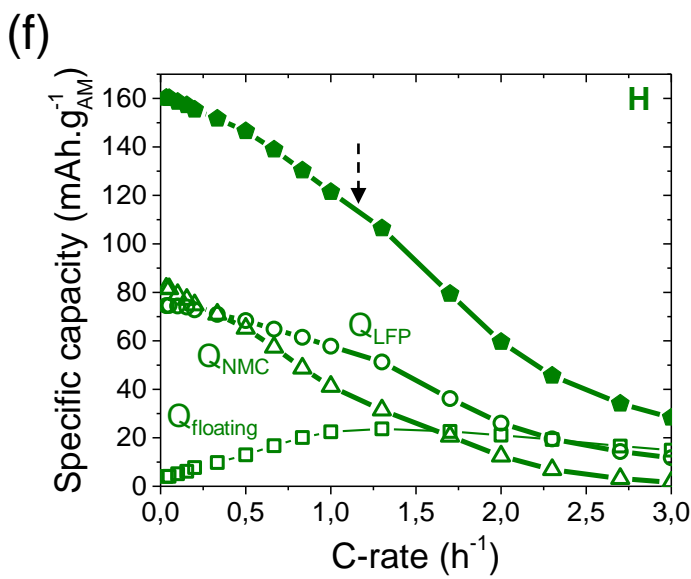
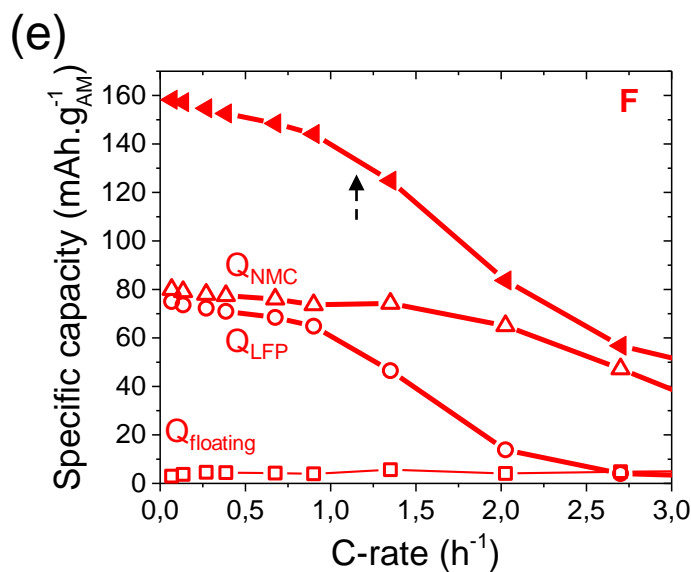
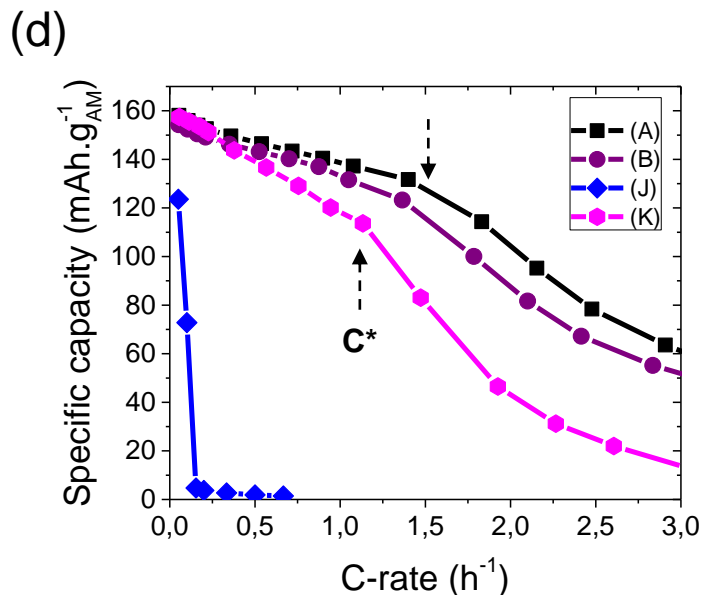
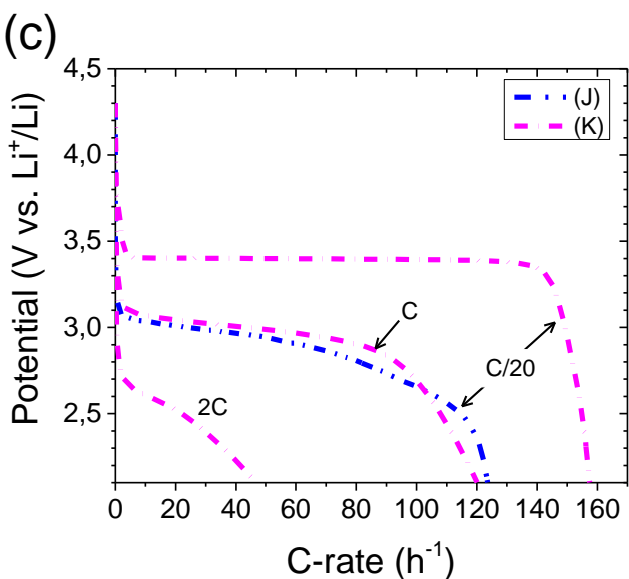
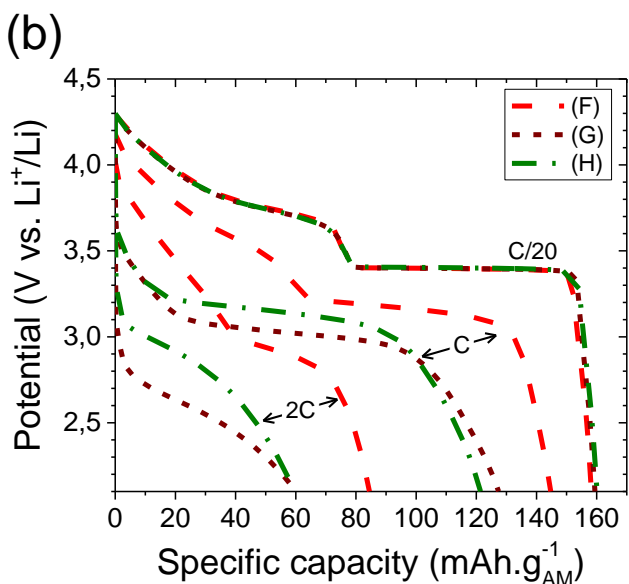
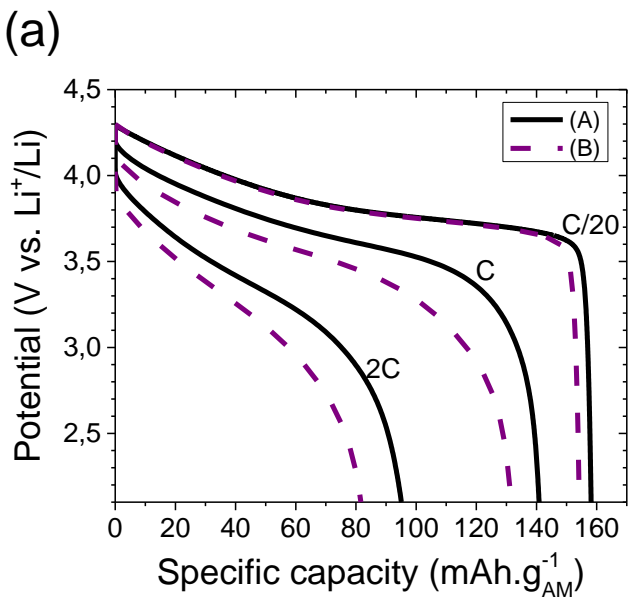
**H**



# Figure 3

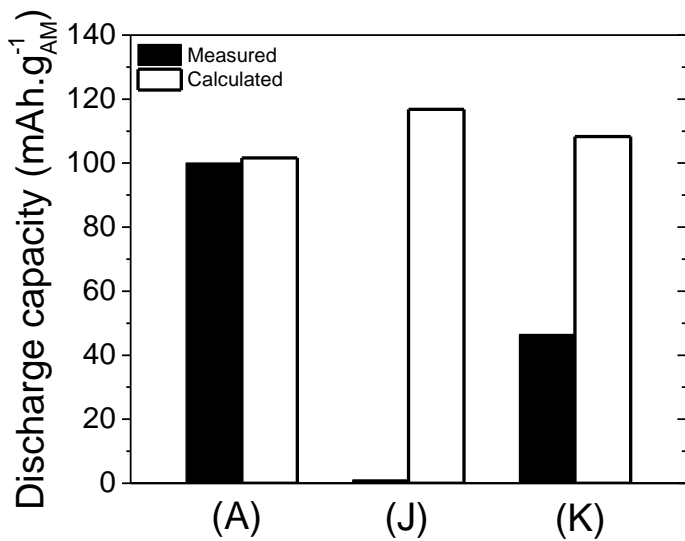


**Figure 4**

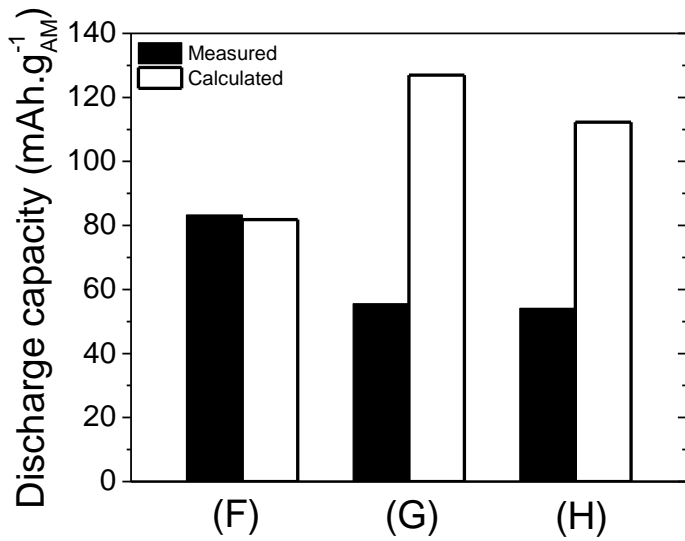
**Figure 5**

# Figure 6

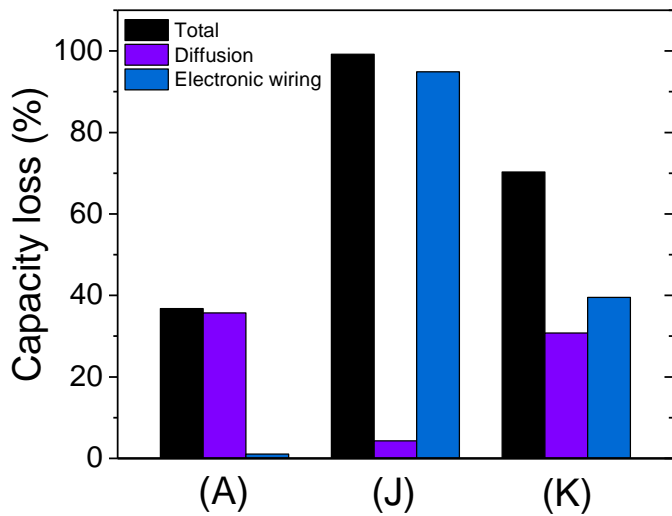
(a)



(b)



(c)



(d)

